



Search for massive long-lived particles decaying semileptonically at $\sqrt{s} = 13 \text{ TeV}$

LHCb Collaboration*

CERN, 1211 Geneva 23, Switzerland

Received: 18 October 2021 / Accepted: 6 March 2022 / Published online: 28 April 2022
© CERN for the benefit of the LHCb collaboration 2022

Abstract A search is performed for massive long-lived particles (LLPs) decaying semileptonically into a muon and two quarks. Two kinds of LLP production processes were considered. In the first, a Higgs-like boson with mass from 30 to $200 \text{ GeV}/c^2$ is produced by gluon fusion and decays into two LLPs. The analysis covers LLP mass values from $10 \text{ GeV}/c^2$ up to about one half the Higgs-like boson mass. The second LLP production mode is directly from quark interactions, with LLP masses from 10 to $90 \text{ GeV}/c^2$. The LLP lifetimes considered range from 5 to 200 ps. This study uses LHCb data collected from proton-proton collisions at $\sqrt{s} = 13 \text{ TeV}$, corresponding to an integrated luminosity of 5.4 fb^{-1} . No evidence of these long-lived states has been observed, and upper limits on the production cross-section times branching ratio have been set for each model considered.

1 Introduction

Supersymmetry (SUSY) is one of the most popular extensions of the Standard Model (SM), which can solve the hierarchy problem, can unify the gauge couplings at the Planck scale and proposes dark matter candidates. The minimal supersymmetric extension of the Standard Model (MSSM) is the simplest phenomenologically viable realisation of SUSY [1, 2]. The present study addresses a subset of models featuring massive long-lived particles (LLPs) with a measurable flight distance [3, 4], decaying semileptonically. Long-lived particles decaying semileptonically with displaced jets composed of SM particles have been studied by the experiments at the LHC [5–9]. Additional information on searches for LLPs at collider experiments can be found in Refs. [10–12].

This analysis uses proton-proton (pp) collision data at a centre-of-mass energy $\sqrt{s} = 13 \text{ TeV}$ collected by the LHCb experiment at the LHC, corresponding to a total integrated luminosity of 5.4 fb^{-1} . It extends the analysis of Ref. [9]

on data collected at $\sqrt{s} = 7$ and 8 TeV . The adopted theoretical framework is inspired by the SUper GRAvity (mSUGRA) with R-parity violation (RPV) [13], in which the neutralino can decay into a muon and two quarks: $\tilde{\chi}_1^0 \rightarrow \mu^+ q_i q_j (\mu^- \bar{q}_i \bar{q}_j)$. Neutralinos can be produced by a variety of processes. In this paper the analysis has been performed assuming the two mechanisms depicted in Fig. 1. In the first process, a Higgs-like particle, h^0 , is produced by gluon fusion and decays into two LLPs. The analysis covers h^0 masses from 30 to $200 \text{ GeV}/c^2$, LLP lifetimes from 5 to 200 ps and LLP mass values from $10 \text{ GeV}/c^2$ up to about one half the h^0 mass. The second mode is a direct LLP production from quark interactions. The LLP lifetime range considered is from 5 to 200 ps and the mass range from 10 to $90 \text{ GeV}/c^2$. The LLP lifetime range begins at 5 ps, well above the typical b-hadron lifetime, and extends up to 200 ps, where most of the vertices are still within the LHCb vertex locator (VELO). The mass range avoids the region of the SM b-quark states, but also takes into account the forward acceptance of the LHCb detector within which the decay products of relatively light LLPs can be efficiently detected.

The LLP signature is a displaced vertex made of charged particle tracks accompanied by an isolated muon with high transverse momentum with respect to the proton beam direction, p_T . This study benefits from the excellent vertex reconstruction provided by the Velo, and by the low p_T threshold of the muon trigger, compared to the other LHC experiments. In addition, the LHCb experiment is probing a rapidity region only partially accessible by other LHC experiments. These properties allow the LHCb experiment to be complementary to similar analyses performed by the two central detectors at the LHC and even explore regions of the theoretical parameter space where these experiments are limited by their low efficiency to reconstruct highly boosted LLPs.

2 Detector description and simulation

The LHCb detector [14, 15] is a single-arm forward spectrometer covering the pseudorapidity range $2 < \eta < 5$,

* e-mail: aurelio.bay@epfl.ch (corresponding author)

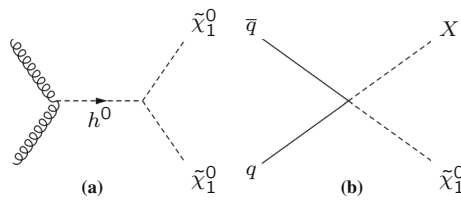


Fig. 1 LLP production processes considered in this paper, where the $\tilde{\chi}_1^0$ represents the LLP: **a** di-LLP production via a scalar particle h^0 ; **b** non-resonant, direct LLP production from quark interactions, where X is a stable particle, with mass identical to the LLP. The LLP decays into a muon and two quarks: $\tilde{\chi}_1^0 \rightarrow \mu^+ q_i q_j (\mu^- \bar{q}_i \bar{q}_j)$

designed for the study of particles containing b or c quarks. The detector includes a high-precision tracking system consisting of the VELO which is a silicon-strip detector surrounding the pp interaction region [16], a large-area silicon-strip detector located upstream of a dipole magnet with a bending power of about 4 Tm, and three stations of silicon-strip detectors and straw drift tubes [17, 18] placed downstream of the magnet. The tracking system provides a measurement of the momentum, p , of charged particles with a relative uncertainty that varies from 0.5% at low momentum to 1.0% at $200\text{ GeV}/c$. The minimum distance of a track to a primary pp collision vertex (PV), the impact parameter, is measured with a resolution of $(15 + 29/p_T)\text{ }\mu\text{m}$, where p_T is in GeV/c . Different types of charged hadrons are distinguished using information from two ring-imaging Cherenkov detectors [19]. Photons, electrons and hadrons are identified by a calorimeter system consisting of scintillating-pad and preshower detectors, an electromagnetic (ECAL) and a hadronic calorimeter (HCAL) [20]. Muons are identified by a system composed of alternating layers of iron and multi-wire proportional chambers [21]. The online event selection is performed by a trigger [22], which consists of a hardware stage, based on information from the calorimeter and muon systems, followed by a software stage, which applies a full event reconstruction. During data taking an alignment and calibration of the detector is performed in near real-time and used in the software trigger [23]. The same alignment and calibration information is propagated to the offline reconstruction.

Simulation is used to model the effects of the detector acceptance and the imposed selection requirements. In the simulation, pp collisions are generated using PYTHIA 8 [24, 25] with a specific LHCb configuration [26] and with parton density functions taken from CTEQ6L [27]. The interaction of the generated particles with the detector, and its response, are implemented using the GEANT4 toolkit [28, 29] as described in Ref. [30]. The simulation includes pileup events with an average of 1.1 pp visible interactions per bunch crossing.

Several sets of signal events have been produced assuming the processes illustrated in Fig. 1, where the $\tilde{\chi}_1^0$ plays the role

of a long-lived particle. For the first process considered, two $\tilde{\chi}_1^0$ particles are obtained from the decay of the Higgs-like boson produced by gluon fusion, $gg \rightarrow h^0 \rightarrow \tilde{\chi}_1^0 \tilde{\chi}_1^0$. For the second process, the LLP is produced in a non-resonant mode, $q\bar{q} \rightarrow \tilde{\chi}_1^0 X$. Here X is a stable neutral particle with the same mass as that of the $\tilde{\chi}_1^0$ state. This production of a LLP in association with a stable particle X is included, which enables probing the sensitivity to this topology, with the signal LLP recoiling against such a particle.

The LLP decays into a muon and two quarks; the branching ratio of $\tilde{\chi}_1^0 \rightarrow \mu^+ q_i q_j (\mu^- \bar{q}_i \bar{q}_j)$ is set to be equal for each quark combination ($q_i = u, c$ and $q_j = \bar{d}, \bar{s}, \bar{b}$), with an equal proportion of μ^+ and μ^- .

In the following, the model name is indicated by the values of m_{h^0} , $m_{\tilde{\chi}_1^0}$ and $\tau_{\tilde{\chi}_1^0}$; h125-chi40-10ps, for example, corresponds to $m_{h^0} = 125\text{ GeV}/c^2$, $m_{\tilde{\chi}_1^0} = 40\text{ GeV}/c^2$, $\tau_{\tilde{\chi}_1^0} = 10\text{ ps}$. For the direct production, the Higgs mass is omitted from this notation, such as for example in chi30-10ps.

The most relevant background in this analysis is from events containing heavy quarks. The background from heavy quarks directly produced in pp collisions, as well as from W , Z , Higgs boson and top quark decays, is studied using the simulation. The simulation of inclusive $b\bar{b}$ and $c\bar{c}$ events is not efficient to produce a large enough sample to cover the relevant high- p_T muon kinematic region. Hence, a dedicated sample of 20×10^6 (1×10^6) simulated $b\bar{b}$ ($c\bar{c}$) events has been produced with a minimum parton \hat{p}_T of $20\text{ GeV}/c$ and requiring a muon with $p_T > 12\text{ GeV}/c$ and $1.5 < \eta < 5.0$. All the simulated background species are suppressed by the multivariate analysis presented in the next section. Therefore, a data-driven approach is employed for the final background estimation.

3 Signal selection

Signal events are selected by requiring a vertex displaced from any PV in the event and containing one isolated, high- p_T muon. Due to the relatively high LLP mass, the muons from the LLP decay are expected to be more isolated than muons from hadron decays. The events from pp collisions are selected online by a trigger requiring muons with $p_T > 10\text{ GeV}/c$. The offline analysis requires that the triggering muon has an impact parameter, IP^μ , with respect to any PV, larger than 0.25 mm and a transverse momentum, p_T^μ , larger than $12\text{ GeV}/c$. Primary and displaced vertices are reconstructed offline from charged particle tracks [31]. Genuine PVs are identified by a small radial distance from the beam axis, $R_{xy} < 0.3\text{ mm}$. Once the set of PVs is identified, all the other vertices are candidates for the decay position of LLPs. An LLP candidate is formed by requiring three or more tracks including the muon and having an invari-

ant mass above $4.5 \text{ GeV}/c^2$. There is no requirement for the reconstructed momentum to point to a specific PV. Particles interacting with the detector material are an important source of background. Therefore, a geometric veto is used to reject candidates with vertices in regions occupied by detector material [32]. The event preselection requires at least one PV in the event and at least one LLP candidate.

Figure 2 compares the distributions from data and from the simulated $b\bar{b}$ events for the relevant observables, after preselection. For illustration the shapes of simulated h125-chi40-10ps events are also superimposed. The effect of the geometric veto is visible in the R_{xy} distribution, for candidates with R_{xy} above 5 mm. From simulation, the veto introduces a loss of efficiency of 3% (27%) for the detection of LLPs with a $50 \text{ GeV}/c^2$ mass and a 10 ps (200 ps) lifetime, $m_{h^0} = 125 \text{ GeV}/c^2$. The muon-isolation variable is defined as the sum of the energy of tracks surrounding the muon direction, including the muon itself, in a cone of radius $R_{\eta\phi} = 0.3$ in the pseudorapidity-azimuthal (η, ϕ) space, divided by the energy of the muon track. The radius is reduced to $R_{\eta\phi} = 0.2$ when the theoretical hypothesis assumes a LLP mass of $10 \text{ GeV}/c^2$, to account for the reduced aperture of the jet of particles produced by the LLP decay. A muon-isolation value of unity denotes a fully isolated muon. In simulation the muon from the signal is found to be more isolated than the hadronic background. The variables σ_R and σ_Z are the vertex uncertainties in the radial direction and in the z direction respectively.

The reconstructed vertex mass is very broad and does not peak at the neutralino mass values, because it misses some charged particle tracks, and any neutrals produced in the LLP decay.

The shapes of the distributions in Fig. 2 are all consistent with a dominant $b\bar{b}$ composition of the background. This is confirmed by comparing the yields in data and simulation: after preselection and requiring the isolation parameter below 1.2, the total number of LLP candidates in data is 148×10^3 . The predicted background yields from $b\bar{b}$ and $c\bar{c}$ events are $(120 \pm 20) \times 10^3$ and $(14 \pm 4) \times 10^3$, respectively. Small contributions are expected from processes with W, Z bosons plus jets, top and Standard Model Higgs events: 260, 20, 2, and 1 candidates, respectively. The $b\bar{b}$ and $c\bar{c}$ prediction uses the cross-sections measured by the LHCb experiment at 13 TeV [33, 34]. The acceptance of this analysis is computed with MADGRAPH5- AMC@NLO [35] and the detection efficiency is obtained from simulated events. As already stated, these background estimations are only used for cross-checks.

A multivariate analysis (MVA) based on a boosted decision tree [36, 37] is used to further purify the data sample. Ten MVA input variables are selected to optimise the signal-background separation. They are: p_T^μ and IP^μ , the ratio of the energies associated with the muon measured in ECAL and HCAL normalised to the muon energy, the LLP candi-

date p_T , its pseudorapidity, the number of tracks forming the LLP, the vertex uncertainties σ_R and σ_Z , and the vertex R_{xy} distance.

Larger vertex uncertainties are expected on the vertices of candidates from $b\bar{b}$ events compared to signal LLPs. The former are more boosted and produce more collimated tracks, while the relatively heavier signal LLPs decay into more divergent tracks. This effect decreases when the mass of the LLP approaches the mass of b -quark hadrons. The selection based on the energy deposit in the calorimeters is efficient to suppress the background due to kaons or pions punching through the calorimeters and being misidentified as muons. The muon-isolation variable and the reconstructed mass of the long-lived particles are not included in the classifier; the discrimination power of these two variables is subsequently exploited for the signal determination.

The signal MVA training samples are provided by simulation. The background training sample is obtained from data, based on the hypothesis that the fraction of signal in the data after preselection is small. This automatically includes all possible background sources, with the correct relative abundance.

The training is performed independently for each simulated model. The MVA classifier is subsequently applied to the data and to the simulated signal. For each model, the optimal MVA cut value is chosen by an iterative minimization procedure to give the best expected cross-section upper limit, but keeping at least ten candidates to allow the invariant-mass fit to work properly.

The classifier can be biased by the presence of signal in data used as background training set. To quantify the potential bias, the MVA training is performed adding a fraction of simulated signal events (up to 5%) to the background set. This test demonstrates a negligible effect on the MVA performance for all the signal models.

4 Determination of the signal yield

The signal yield is determined with an unbinned extended maximum-likelihood fit to the distribution of the reconstructed LLP mass. The shape of the signal component is taken from the simulated models, and a background component is added. After the MVA selection, no simulated background survives, therefore the background shape is determined by a data-driven method, which also avoids potential simulation mismodeling of the reconstructed mass. The data candidates are separated into a signal region with muon isolation below 1.2 and a background region with isolation values from 1.4 to 2.0. The signal-region selection accepts more than 80% of the signal for all the models considered (see e.g. Fig. 2). Any potential signal yield in the background

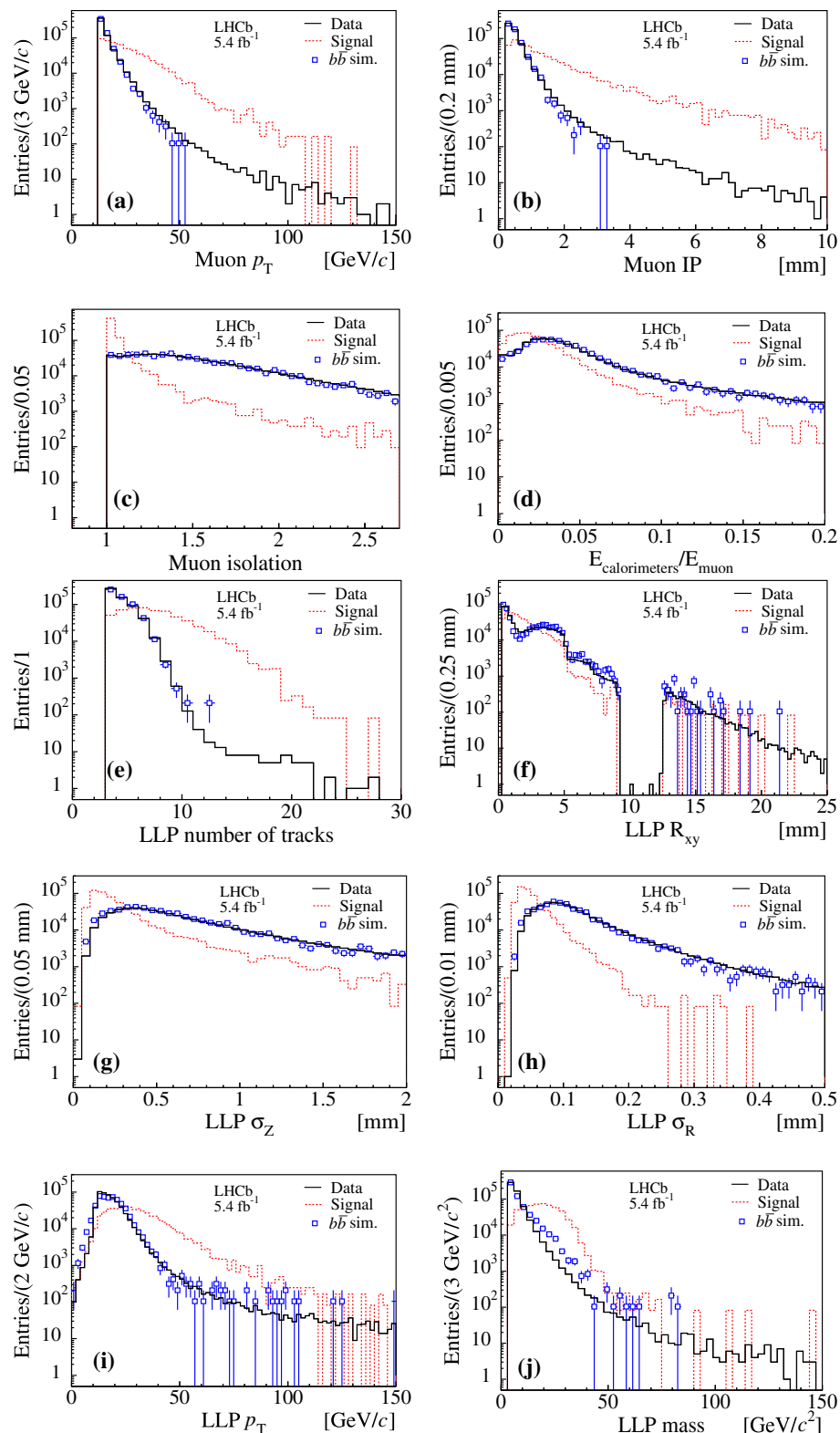


Fig. 2 Distributions from data compared to simulated $b\bar{b}$ events (blue) and the simulated signal $h_{125}\text{-}\chi_{40-10p}$ (red), after preselection. From **a** to **j**: muon transverse momentum; muon impact parameter; muon isolation; the calorimetric energy, $E_{\text{calorimeters}}$, associated with the muon normalised by the muon energy, $E_{\mu\text{on}}$; the number of tracks used to

reconstruct the LLP vertex including the muon; the radial distance to the beam line of the reconstructed vertex; longitudinal and radial vertex fit errors, σ_Z and σ_R ; reconstructed transverse momentum and mass of the LLP candidate. The distributions from simulated events are normalised to the data

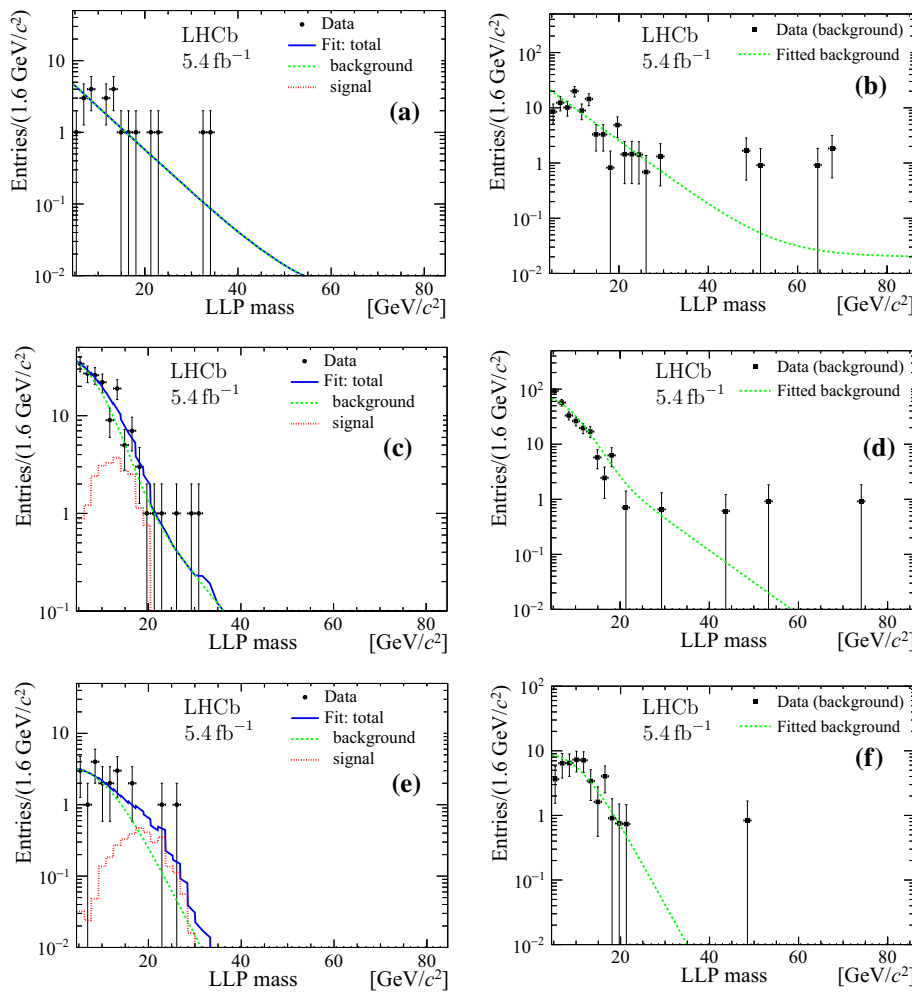


Fig. 3 Reconstructed invariant mass of the LLP candidates. Subfigures **a**, **c**, and **e** correspond to the signal selections which assume the models h80-chi30-10ps, h200-chi20-10ps, and the non-resonant model

chi30-10ps, respectively. Subfigures **b**, **d**, and **f** are the corresponding distributions for candidates selected in the background region. The results of the fits are superimposed

region is considered negligible. The reconstructed mass distribution obtained from the background candidates is used to constrain an empirical probability density function (PDF) consisting of the sum of two negative-slope exponential functions, one of them convolved with a Gaussian function. Shape parameters and amplitudes are left to vary in the fit. It is possible that the mass distribution obtained after selection of the background region does not represent exactly the background component in the signal region. Hence, a correction is applied before performing the fit: the mass distribution selected in the background region is weighted with weights deduced from the comparison of the candidate mass distributions of signal and background regions obtained from data with a relaxed MVA selection. This relaxed selection is required to have sufficiently populated samples and to minimise the correlation with the final distributions from which signal yields are

obtained. The consistency of this procedure is tested on $b\bar{b}$ simulated events.

Examples of the invariant mass of the selected LLP candidates are shown in Fig. 3 for the signal and background regions. The invariant-mass fit is performed simultaneously on LLP candidates from the signal and from the background regions. In the former, the numbers of signal and background events are free parameters of the fit. The results of the fit are shown in the figure. The sensitivity of the fit procedure is studied by adding a small number of simulated signal events to the data according to a given signal model. The fitted yields are on average consistent with the numbers of added events. The fitted signal yields, given in Tables 1 and 2 are compatible with the background-only hypothesis for all the theoretical models.

Table 1 Signal detection efficiency, in percent, after preselection, ε_{presel} , including the geometrical acceptance, and after MVA selection, ε , and numbers of fitted signal and background events in the signal region, N_s and N_b , for the different signal hypotheses with resonant LLP production (masses units are GeV/c^2 , lifetimes in ps). The last column gives the value of χ^2 per degree of freedom, ndf, from the fit

m_{h0}	$m_{\tilde{\chi}_1^0}$	τ_{khi}	ε_{presel}	ε	N_b	N_s	χ^2/ndf
30	10	10	0.19	0.03	1025.7 ± 159.4	-89.7 ± 39.1	2.75
41	10	10	0.29	0.01	61.3 ± 51.7	-5.3 ± 5.2	0.67
41	20	10	0.53	0.08	73.2 ± 14.2	13.8 ± 12.8	1.22
50	10	10	0.46	0.09	1421.3 ± 84.4	-71.4 ± 75.1	1.03
50	20	10	0.95	0.12	18.3 ± 6.9	6.7 ± 6.4	1.12
80	10	10	0.74	0.05	127.0 ± 17.8	1.0 ± 14.5	1.35
80	20	10	1.86	0.42	53.9 ± 45.3	-5.4 ± 5.0	1.07
80	30	10	2.34	0.72	22.4 ± 4.2	-0.4 ± 4.2	0.67
80	40	10	1.83	0.43	12.1 ± 4.1	1.9 ± 4.5	0.53
125	10	5	0.63	0.04	333.7 ± 28.0	-10.6 ± 21.7	0.77
125	10	10	0.68	0.06	198.3 ± 19.2	4.7 ± 14.7	1.72
125	10	20	0.73	0.09	1680.8 ± 42.9	-172.2 ± 34.0	0.96
125	10	30	0.64	0.08	419.0 ± 45.1	-29.9 ± 34.8	1.43
125	10	40	0.49	0.06	184.7 ± 30.4	8.3 ± 28.2	0.77
125	10	50	0.51	0.11	667.0 ± 46.9	-2.0 ± 39.5	1.20
125	10	100	0.32	0.04	53.7 ± 12.4	10.3 ± 11.7	1.14
125	10	200	0.19	0.03	71.5 ± 8.4	-0.5 ± 4.1	0.57
125	20	5	1.86	0.36	56.1 ± 43.3	-5.8 ± 5.6	1.27
125	20	10	2.28	0.67	39.6 ± 36.8	-3.9 ± 5.4	1.06
125	20	20	2.24	0.47	18.1 ± 15.4	-0.1 ± 5.5	0.97
125	20	30	2.10	0.35	9.5 ± 4.0	7.5 ± 4.2	0.93
125	20	50	1.73	0.44	28.9 ± 9.4	8.1 ± 8.7	1.67
125	20	80	1.36	0.21	22.9 ± 5.8	2.1 ± 5.5	0.24
125	20	100	1.18	0.25	15.0 ± 14.9	-1.0 ± 4.1	0.80
125	20	200	0.71	0.09	11.0 ± 2.0	-3.5 ± 2.2	0.40
125	30	5	2.24	0.68	93.5 ± 8.8	-15.0 ± 5.5	2.26
125	30	10	3.13	0.72	7.0 ± 4.0	3.9 ± 4.0	0.84
125	30	20	3.24	0.93	6.6 ± 3.2	3.4 ± 3.1	0.35
125	30	30	2.92	0.87	14.3 ± 2.9	-1.6 ± 2.8	0.84
125	30	50	2.51	1.00	22.7 ± 22.6	-1.7 ± 6.2	0.83
125	30	100	1.84	0.58	8.8 ± 5.5	-2.7 ± 2.1	0.96
125	30	200	1.09	0.45	25.3 ± 4.8	-4.8 ± 4.1	1.16
125	40	5	2.41	0.59	9.9 ± 6.3	-2.5 ± 1.9	0.77
125	40	10	3.44	0.84	11.0 ± 1.6	-2.2 ± 2.1	0.94
125	40	20	3.79	1.90	10.5 ± 3.2	4.5 ± 2.6	0.72
125	40	30	3.71	1.37	6.3 ± 3.4	4.7 ± 3.4	1.31
125	40	50	3.24	1.39	28.6 ± 1.7	-10.6 ± 4.8	0.87
125	40	100	2.30	0.64	9.9 ± 8.3	-1.4 ± 2.2	0.56
125	40	200	1.49	0.61	9.9 ± 8.1	-1.5 ± 2.2	1.28
125	50	5	2.25	0.48	8.3 ± 1.5	-0.3 ± 2.4	0.60
125	50	10	3.41	1.60	20.9 ± 4.0	1.1 ± 1.8	0.58
125	50	20	4.10	2.01	16.5 ± 0.5	-14.9 ± 11.9	0.57
125	50	30	4.13	2.04	4.2 ± 2.4	3.9 ± 2.5	0.69
125	50	50	3.86	2.30	17.5 ± 0.5	-0.5 ± 0.3	0.64
125	50	100	3.02	1.74	15.4 ± 0.8	-9.3 ± 2.9	0.95
125	50	200	2.00	0.90	4.4 ± 1.9	3.5 ± 2.1	0.76
125	60	5	1.64	0.48	20.9 ± 15.8	-2.6 ± 3.1	0.64

Table 1 continued

m_{h0}	$m_{\tilde{\chi}_1^0}$	τ_{khi}	ε_{presel}	ε	N_b	N_s	χ^2/ndf
125	60	10	2.85	1.22	9.8 ± 2.1	-0.8 ± 2.2	1.10
125	60	20	3.98	2.04	22.8 ± 4.8	1.2 ± 1.9	0.88
125	60	30	4.20	2.39	16.5 ± 0.3	-10.0 ± 0.9	0.73
125	60	50	4.57	2.87	20.9 ± 2.9	3.1 ± 1.4	1.13
125	60	100	3.68	2.30	9.9 ± 1.9	-1.3 ± 2.4	1.73
125	60	200	2.75	1.90	10.7 ± 3.8	3.3 ± 3.0	1.58
150	10	10	0.62	0.12	1514.7 ± 52.5	-152.0 ± 30.8	2.01
150	20	10	2.19	0.67	66.0 ± 13.6	-8.2 ± 6.0	1.47
150	30	10	3.20	0.60	6.9 ± 2.0	1.1 ± 1.1	0.67
150	40	10	3.55	1.44	15.4 ± 12.1	-2.1 ± 2.8	1.35
150	50	10	3.79	1.06	6.9 ± 2.0	1.1 ± 1.1	0.87
150	60	10	3.68	1.79	25.3 ± 1.5	-15.0 ± 1.7	1.41
200	10	10	0.46	0.05	433.1 ± 34.2	7.0 ± 27.6	1.59
200	20	10	1.93	0.45	136.2 ± 26.2	21.8 ± 24.5	0.95
200	30	10	2.94	0.48	8.6 ± 3.9	4.4 ± 4.2	0.79
200	40	10	3.43	0.84	9.3 ± 2.8	3.7 ± 2.2	1.30
200	50	10	3.84	1.48	12.1 ± 2.1	-1.8 ± 2.3	0.50
200	60	10	3.97	1.81	12.1 ± 2.1	-1.8 ± 2.5	0.56
200	50	5	2.90	1.20	11.8 ± 2.1	-0.8 ± 1.2	0.57
200	50	20	3.80	1.79	7.7 ± 2.7	1.3 ± 2.8	0.70
200	50	30	3.45	0.98	17.6 ± 1.7	-6.0 ± 2.7	0.62
200	50	50	2.91	1.14	7.7 ± 0.8	-3.4 ± 1.9	1.07
200	50	100	1.95	1.04	10.0 ± 3.0	1.0 ± 3.0	1.07
200	50	200	1.17	0.72	17.6 ± 3.5	-4.0 ± 3.6	0.50

Table 2 Signal detection efficiency, in percent, after preselection, ε_{presel} , including the geometrical acceptance, and after MVA selection, ε , and numbers of fitted signal and background events in the signal region, N_s and N_b , for the different signal hypotheses for the LLP non-resonant production models (masses units are GeV/c^2 , lifetimes in ps). The last column gives the value of χ^2 per degree of freedom, ndf, from the fit

$m_{\tilde{\chi}_1^0}$	$\tau_{\tilde{\chi}_1^0}$	ε_{presel}	ε	N_b	N_s	χ^2/ndf
10	10	0.61	0.13	2767.9 ± 88.2	-141.8 ± 69.7	1.69
20	10	0.66	0.23	43.9 ± 40.1	-4.2 ± 5.0	0.67
30	10	2.29	0.47	15.7 ± 5.8	3.3 ± 5.2	0.90
40	10	2.49	0.52	1.1 ± 1.4	5.9 ± 2.8	0.96
60	10	3.81	1.97	45.1 ± 5.6	-8.0 ± 4.3	0.80
90	10	2.52	1.68	30.8 ± 2.2	-9.8 ± 5.0	1.04
30	5	1.44	0.21	11.0 ± 2.5	-1.0 ± 2.7	0.67
30	20	2.64	0.66	13.8 ± 4.4	3.2 ± 4.2	0.65
30	30	2.52	0.74	5.6 ± 2.2	2.4 ± 2.1	0.41
30	50	2.25	0.81	16.5 ± 16.1	-1.8 ± 3.2	0.69
30	100	1.68	0.61	9.9 ± 7.4	-1.7 ± 3.1	1.10
30	200	1.06	0.29	38.0 ± 6.3	-0.0 ± 2.3	0.79

5 Detection efficiency and systematic uncertainties

The detection efficiency required in the calculation of the signal yield is estimated from the simulated signal events. The efficiencies after preselection and after MVA selection are shown in Tables 1 and 2, for the considered models of resonant and non-resonant LLP productions, respectively.

The values include the geometrical acceptance. Several phenomena compete to determine the detection efficiency. In general the efficiency after preselection increases with the LLP mass because more particles are produced in the decay of heavier LLPs. There is a loss of particles outside the spectrometer acceptance, especially when the LLPs are produced from the decay of heavier states, such as the Higgs-like

Table 3 Contributions to the relative systematic uncertainties. The indicated ranges cover the theoretical models considered. The contributions from the signal and background models used in the LLP mass fit are treated separately

Source	Contribution [%]
Integrated luminosity	2.0
Parton luminosity gluons fusion (quarks)	6.0 (3.0)
Simulation statistics	2.0–4.0
Muon reconstruction	2.0–3.7
p_T^μ	1.0
IP $^\mu$	1.0
Vertex reconstruction	2.0
Beam line uncertainty (R_{xy})	0.9
Muon isolation	1.7
MVA	1.7–16
Mass calibration	1.4
Total	7.3–18.9

particle. In addition, the lower boost of heavier LLPs results in a shorter average flight length, which is disfavoured by the requirement of a minimum R_{xy} value. With increasing LLP lifetimes a larger portion of the decays falls into the material region and is vetoed. Finally, a drop of sensitivity is expected for LLPs with a lifetime close to the b -hadron lifetimes, where the contamination from $b\bar{b}$ events becomes even more important, especially for low-mass LLPs. The detection efficiency is reduced by up to one order of magnitude after the optimised MVA selection while the background is reduced by 3–4 orders of magnitude.

A breakdown of the relative systematic uncertainties is shown in Table 3. The uncertainties of the partonic luminosity depend upon the process considered; they are estimated following the procedure explained in Refs. [38, 39] and vary from 3% up to 6%, which is found for the gluon fusion process. The integrated luminosity [40] contributes with an uncertainty of 2%. The statistical precision of the efficiencies determined from simulation is in the range 2–4% for the different models. Different sources of systematic uncertainty arising from discrepancies between data and simulation have been considered. The size of those discrepancies for the relevant observables are inferred from a comparison of the distributions obtained from data and from $b\bar{b}$ simulated events, which describes the data quite completely, or from other calibration processes.

The muon detection efficiency, including trigger, tracking, and muon identification efficiencies, is studied by a tag-and-probe technique applied to muons from $J/\psi \rightarrow \mu^+\mu^-$, $\Upsilon(1S) \rightarrow \mu^+\mu^-$ and $Z \rightarrow \mu^+\mu^-$ decays. The corresponding systematic effects due to differences between data and simulation are estimated to be between 2 and 3.7%, depending on the theoretical model considered.

Table 4 Upper limits at 95% CL on the production cross-section times branching ratio for signal models with a resonant production via an Higgs-like boson. Masses are given in GeV/c^2 , lifetimes in ps, cross-sections in pb

m_{h^0}	$m_{\tilde{\chi}_1^0}$	$\tau_{\tilde{\chi}_1^0}$	Expected UL	$-\sigma$	$+\sigma$	Observed UL
30	10	10	40.24	16.52	31.86	28.34
41	10	10	30.89	11.41	41.72	22.37
41	20	10	7.95	2.24	3.55	10.07
50	10	10	13.72	4.39	11.90	17.37
50	20	10	2.65	0.82	1.67	3.46
80	10	10	13.72	4.36	9.37	14.00
80	20	10	0.81	0.26	0.40	0.64
80	30	10	0.36	0.10	0.18	0.29
80	40	10	0.48	0.12	0.20	0.56
125	10	5	22.06	6.37	32.95	21.53
125	10	10	17.76	0.26	15.73	18.08
125	10	20	20.64	7.89	16.67	12.49
125	10	30	17.21	5.37	13.22	15.40
125	10	40	11.10	4.01	9.27	20.91
125	10	50	8.11	2.63	6.80	13.42
125	10	100	7.89	2.74	5.99	16.99
125	10	200	7.50	1.13	8.19	7.82
125	20	5	1.38	0.45	0.60	0.89
125	20	10	0.56	0.15	0.22	0.47
125	20	20	0.49	0.13	0.22	0.55
125	20	30	0.73	0.21	0.34	0.87
125	20	50	0.91	0.21	0.32	1.00
125	20	80	1.11	0.20	0.40	1.11
125	20	100	0.82	0.22	0.38	0.72
125	20	200	0.94	0.38	0.77	0.98
125	30	5	0.55	0.15	0.23	0.30
125	30	10	0.18	0.04	0.09	0.25
125	30	20	0.20	0.05	0.08	0.23
125	30	30	0.22	0.06	0.09	0.19
125	30	50	0.34	0.07	0.11	0.29
125	30	100	0.17	0.06	0.11	0.17
125	30	200	0.48	0.15	0.17	0.46
125	40	5	0.18	0.06	0.10	0.15
125	40	10	0.17	0.05	0.08	0.14
125	40	20	0.10	0.02	0.04	0.11
125	40	30	0.16	0.04	0.06	0.17
125	40	50	0.18	0.05	0.07	0.14
125	40	100	0.20	0.06	0.11	0.20
125	40	200	0.23	0.07	0.11	0.20
125	50	5	0.28	0.08	0.13	0.35
125	50	10	0.07	0.02	0.04	0.07
125	50	20	0.05	0.02	0.03	0.04
125	50	30	0.09	0.02	0.04	0.10
125	50	50	0.08	0.02	0.03	0.09
125	50	100	0.07	0.03	0.04	0.05

Table 4 continued

m_{h^0}	$m_{\tilde{\chi}_1^0}$	$\tau_{\tilde{\chi}_1^0}$	Expected UL	$-\sigma$	$+\sigma$	Observed UL
125	50	200	0.18	0.04	0.08	0.20
125	60	5	0.49	0.13	0.21	0.49
125	60	10	0.11	0.03	0.05	0.10
125	60	20	0.05	0.02	0.03	0.06
125	60	30	0.04	0.01	0.03	0.03
125	60	50	0.06	0.02	0.03	0.06
125	60	100	0.07	0.02	0.03	0.07
125	60	200	0.15	0.02	0.06	0.14
150	10	10	14.85	5.52	9.07	9.81
150	20	10	0.60	0.18	0.35	0.41
150	30	10	0.15	0.05	0.09	0.16
150	40	10	0.10	0.03	0.05	0.09
150	50	10	0.08	0.03	0.05	0.09
150	60	10	0.04	0.02	0.03	0.04
200	10	10	22.48	6.43	14.67	28.12
200	20	10	2.47	0.61	0.85	2.71
200	30	10	0.48	0.12	0.19	0.53
200	40	10	0.19	0.05	0.09	0.22
200	50	10	0.08	0.03	0.05	0.07
200	60	10	0.07	0.02	0.04	0.06
200	50	5	0.12	0.04	0.06	0.12
200	50	20	0.09	0.02	0.04	0.09
200	50	30	0.12	0.04	0.07	0.11
200	50	50	0.08	0.03	0.05	0.07
200	50	100	0.15	0.04	0.08	0.16
200	50	200	0.19	0.06	0.12	0.20

A comparison of the simulated and observed p_T distributions of muons from $Z \rightarrow \mu^+ \mu^-$ decays shows a maximum difference of 0.2 GeV/c in the selected region; this difference is propagated to the LLP analysis by shifting the muon p_T threshold by the same amount. The corresponding systematic uncertainty is below 1% for all models under consideration.

The muon impact-parameter distribution is also studied from Z decays and shows a discrepancy between data and simulation of about 10 μm close to the p_T^μ threshold. By changing the minimum IP $^\mu$ requirement by this amount, the change in the detection efficiency is below 1% for all the models.

The vertex reconstruction efficiency has a complicated spatial structure due to the geometry of the VELO and the material veto. Uncertainties in the estimated vertex-finding efficiency are due to the per-track efficiency, track resolution, and differences in the contribution from background tracks due to the underlying interaction and pile-up. In the material-free region, $R_{xy} < 4.5$ mm, the efficiency as a function of the flight distance has been studied in the context of lifetime

Table 5 Upper limits at 95% CL on the production cross-section times branching ratio for signal models with a non-resonant production. Masses are given in GeV/c^2 , lifetimes in ps, cross-sections in pb

$m_{\tilde{\chi}_1^0}$	$\tau_{\tilde{\chi}_1^0}$	Expected UL	$-\sigma$	$+\sigma$	Observed UL
10	10	23.67	6.31	12.90	28.84
20	10	0.92	0.24	0.46	0.82
30	10	0.49	0.12	0.19	0.50
40	10	0.31	0.09	0.14	0.44
60	10	0.08	0.03	0.04	0.06
90	10	0.10	0.03	0.05	0.08
30	5	0.86	0.24	0.40	0.90
30	20	0.32	0.08	0.13	0.36
30	30	0.19	0.05	0.09	0.20
30	50	0.22	0.06	0.09	0.20
30	100	0.11	0.04	0.07	0.13
30	200	0.36	0.12	0.23	0.33

measurements [41], showing that the simulation reproduces the data within 1%. In the region $R_{xy} > 4.5$ mm a deviation of less than 6% is inferred from the study of inclusive $b\bar{b}$ events in data and simulation. By altering the efficiency in the simulation program as a function of the true vertex position, the effect on the LLP detection efficiency is estimated to be 1–2%. A second method to determine this contribution uses vertices from $B^0 \rightarrow J/\psi K^{*0}$ decays with $J/\psi \rightarrow \mu^+ \mu^-$ and $K^{*0} \rightarrow K^+ \pi^-$. For this process the vertex detection efficiencies in data and simulation agree within 10%. This result, obtained from a process with four final-state particles, is propagated to the LLP decay into a larger number of charged particle tracks and a detection threshold of three tracks. A discrepancy of at most 2% between the LLP efficiency in data and simulation is found, which is adopted as a contribution to the systematic detection uncertainty.

The uncertainty on the position of the beam line in the transverse plane is less than 20 μm [16]. It can affect the secondary-vertex selection, mainly via the requirement on R_{xy} . By altering the PV position in simulated signal events, the effect is estimated to be below 1%.

The effect of the imperfect modelling on the observables used in the MVA training is estimated with pseudoexperiments. As previously stated, the bias on each input variable is determined by comparing simulated and experimental distributions of muons and LLP candidates from Z and W events, as well as from $b\bar{b}$ events. At the MVA test stage, each input variable is modified by a scale factor randomly selected from a Gaussian distribution of width equal to the corresponding bias. The standard deviation of the signal efficiency distribution is taken as a systematic uncertainty.

The signal and background samples are obtained through a selection on the muon isolation parameter. By a comparison

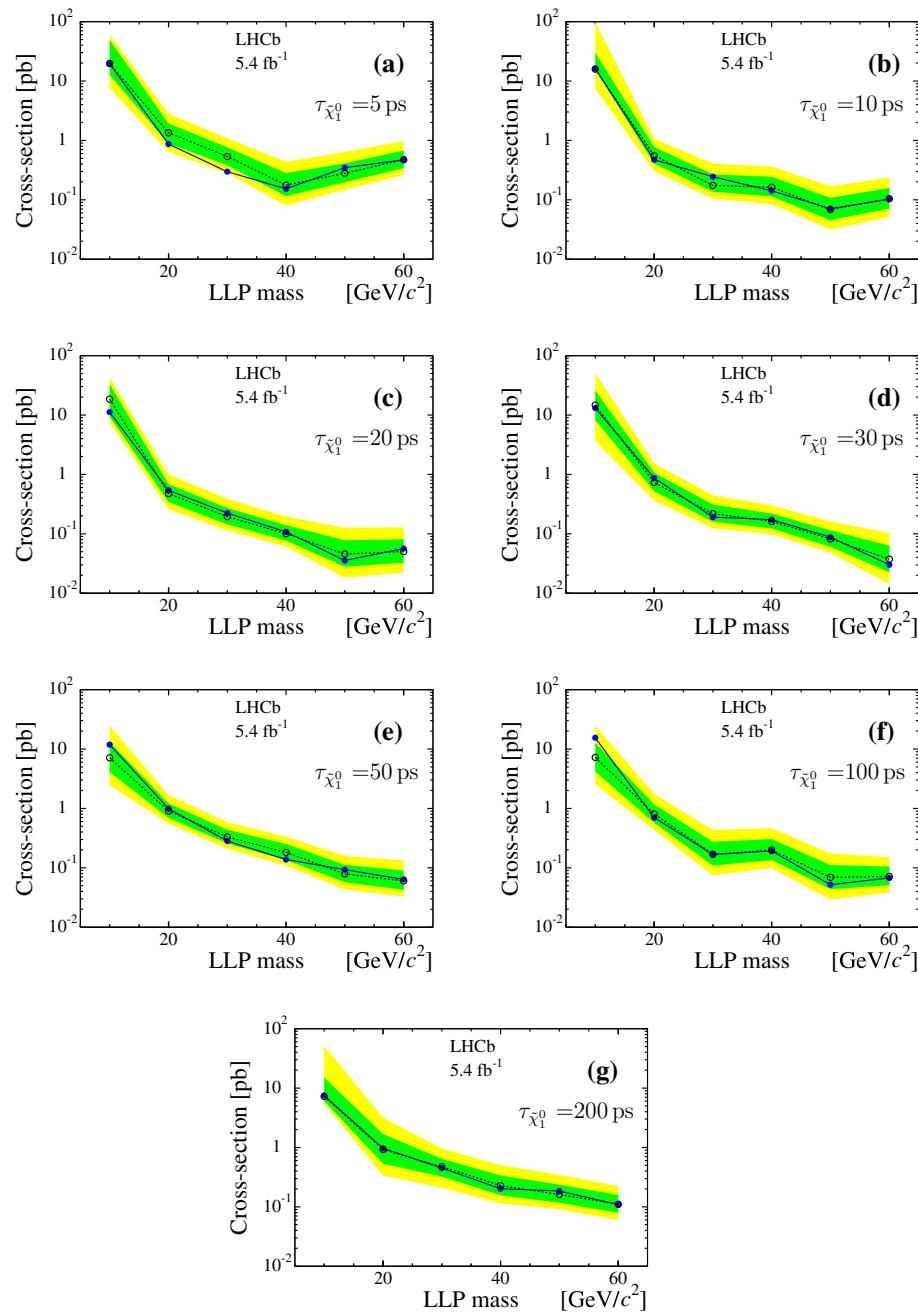


Fig. 4 Expected (open dots and 1σ and 2σ bands) and observed (full dots) cross-section times branching fraction upper limits (95% CL) as a function of $m_{\tilde{\chi}_1^0}$ for the resonant production processes with $m_{h^0} = 125 \text{ GeV}/c^2$, and, from **a** to **g**, $\tau_{\tilde{\chi}_1^0}$ of 5, 10, 20, 30, 50, 100, and 200 ps

of data and muons from simulated $b\bar{b}$ events, the maximum uncertainty on this variable is estimated to be ± 0.015 in the proximity of the thresholds, with a maximal effect on the efficiency of 1.7%.

Comparing the mass distributions of $b\bar{b}$ and $Z \rightarrow b\bar{b}$ events, a maximum mass-scale discrepancy between data and simulated events of 10% is estimated in the proximity of the threshold, which translates into a 1.4% contribution to the detection efficiency uncertainty.

Finally, the total systematic uncertainty is obtained as the sum in quadrature of all contributions, where the different components of the detection efficiency are assumed to be fully correlated.

The choice of the signal and background invariant-mass templates can affect the results of the LLP mass fits. The uncertainty due to the signal model accounts for the mass scale and the mass resolution. The mass scale and resolution discrepancies between data and simulation are below

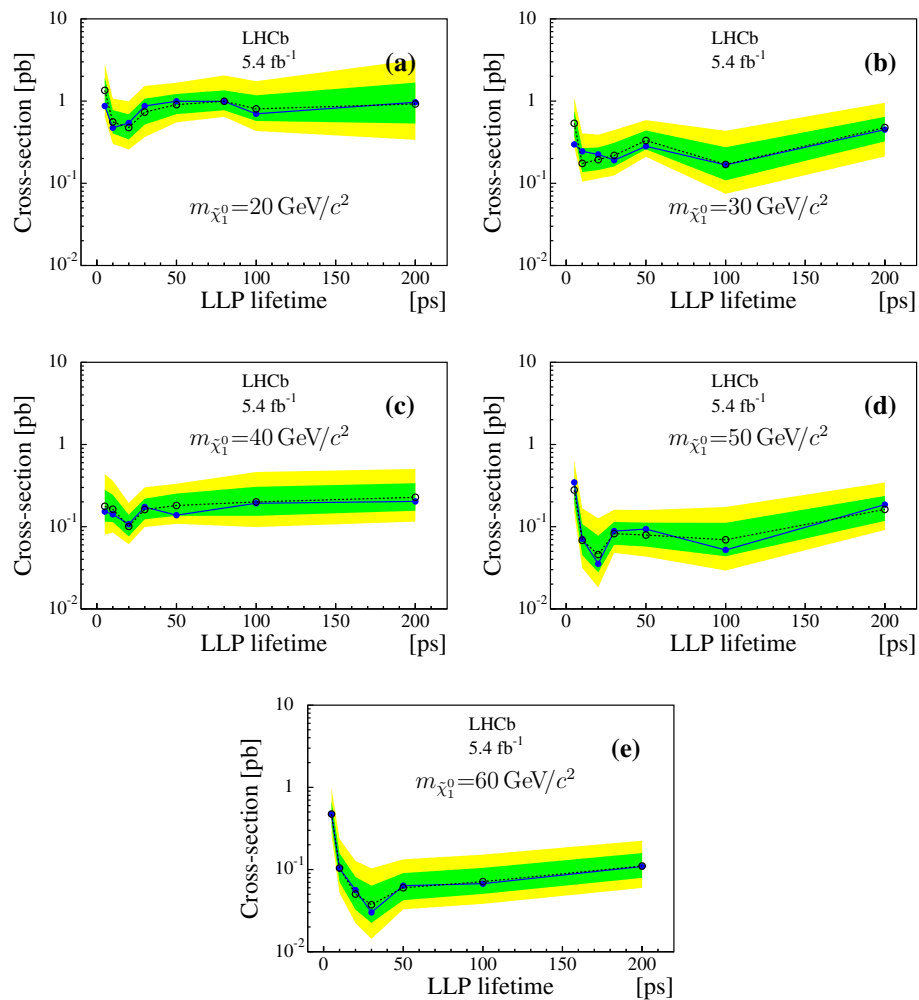


Fig. 5 Expected (open dots and 1σ and 2σ bands) and observed (full dots) cross-section times branching fraction upper limits (95% CL) as a function of $\tau_{\tilde{\chi}_1^0}$ for the resonant production with $m_{h^0} = 125 \text{ GeV}/c^2$, and, from **a** to **e**, $m_{\tilde{\chi}_1^0}$ of 20, 30, 40, 50, and $60 \text{ GeV}/c^2$

1% and 1.5% respectively, as obtained from $b\bar{b}$ and $Z \rightarrow b\bar{b}$ events. Pseudoexperiments are used to estimate the effect on the cross-section calculation. For each theoretical model, ten simulated signal events are added to the selected data after a Gaussian smearing or after changing the mass scale. The average deviation of the observed upper limits with respect to the one obtained from the default signal and background distributions is below 2%.

The background shape is deduced from data selected in the poorly isolated region after reweighting, with weights inferred from the data distributions obtained with relaxed selection criteria. The overall uncertainty is estimated by reducing by half the weights and running pseudoexperiments as before. The average deviation of the observed upper limits is below 14%.

6 Results

The 95% confidence level (CL) upper limits, expected and observed, on the production cross-sections times branching fraction are computed for each model using the CLs approach [42]. Statistical and systematic uncertainties on the signal efficiencies are included as nuisance parameters of the likelihood function, assuming Gaussian distributions. Finally, the upper limit values are corrected by the factors which account for the imperfect modelling of signal and background templates.

The numerical results for all the models are given in Tables 4 and 5. Figures 4, 5, 6 and 7 show the measured cross-section times branching ratio upper limits, for different theoretical models. The decrease of sensitivity for relatively low

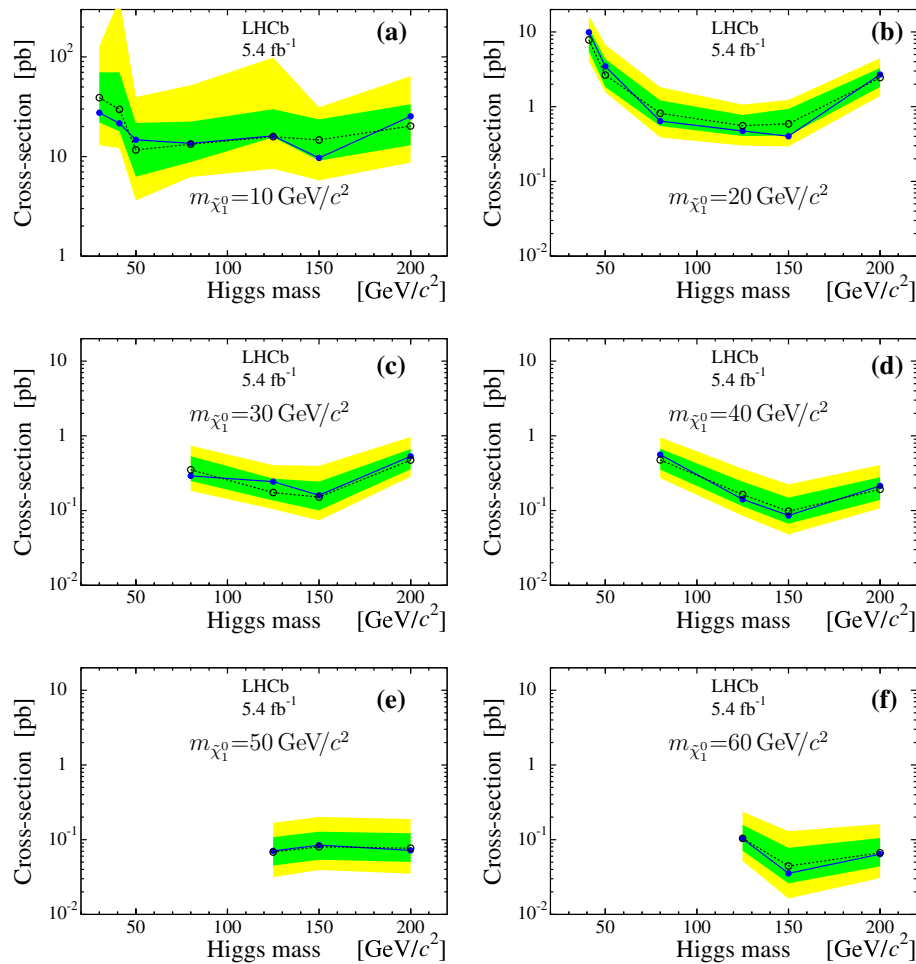


Fig. 6 Expected (open dots and 1σ and 2σ bands) and observed (full dots) cross-section times branching fraction upper limits (95% CL) as a function of m_{h^0} and, from **a** to **f**, $m_{\tilde{\chi}_1^0}$ of 10, 20, 30, 40, 50, and $60 \text{ GeV}/c^2$

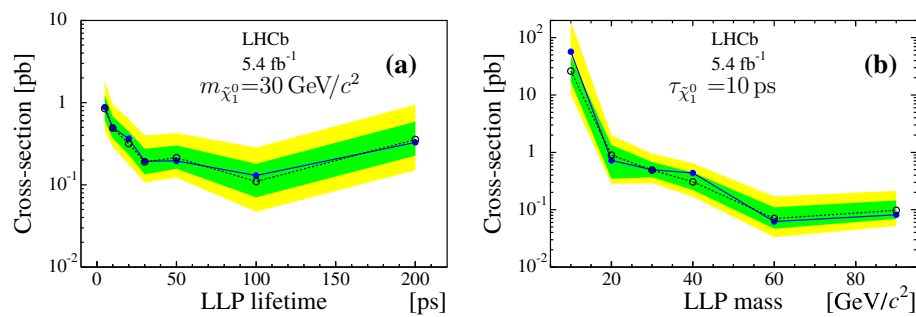


Fig. 7 Expected (open dots and 1σ and 2σ bands) and observed (full dots) cross-section times branching fraction upper limits (95% CL), **a**: as a function of $\tau_{\tilde{\chi}_1^0}$ with $m_{\tilde{\chi}_1^0} = 30 \text{ GeV}/c^2$, **b**: as a function of $m_{\tilde{\chi}_1^0}$ with $\tau_{\tilde{\chi}_1^0} = 10 \text{ ps}$. The processes are from direct, non-resonant, LLP production

LLP mass value is explained by the above-mentioned effects on the detection efficiency. The upper limits for the processes with $m_{h^0} = 125 \text{ GeV}/c^2$ can be compared to the prediction of the Standard Model Higgs production cross-section from gluon fusion of about 46 pb at $\sqrt{s} = 13 \text{ TeV}$ [43].

7 Conclusion

Long-lived massive particles decaying into a muon and two quarks have been searched for using proton-proton collision data collected by the LHCb experiment at $\sqrt{s} = 13 \text{ TeV}$, corresponding to an integrated luminosity of 5.4 fb⁻¹. The LLP lifetime range considered is from 5 to 200 ps. The background is dominated by $b\bar{b}$ events and is reduced by tight selection requirements, including a dedicated multivariate classifier. The signal yield is determined by a fit to the LLP reconstructed mass with a signal shape inferred from the theoretical models.

The forward acceptance of the LHCb experiment makes it complementary to other LHC experiments, while its low trigger p_T threshold allows exploring relatively small LLP masses. Two types of LLP productions have been assumed. In the first a Higgs-like particle is produced by gluon fusion and decays into two LLPs. The analysis covers Higgs-like boson masses from 30 to 200 GeV/ c^2 , and LLP mass range from 10 GeV/ c^2 up to about one half of the mass of the parent boson. The second mode is a direct LLP production from quark interactions, covering the LLP mass range from 10 up to 90 GeV/ c^2 .

The results for all theoretical models considered are compatible with the background-only hypothesis. The upper limits at 95% CL set on the cross-section times branching fractions are mostly of $O(0.1 \text{ pb})$, but the sensitivity is limited to $O(10 \text{ pb})$ for the lowest LLP mass value considered of 10 GeV/ c^2 .

Acknowledgements We express our gratitude to our colleagues in the CERN accelerator departments for the excellent performance of the LHC. We thank the technical and administrative staff at the LHCb institutes. We acknowledge support from CERN and from the national agencies: CAPES, CNPq, FAPERJ and FINEP (Brazil); MOST and NSFC (China); CNRS/IN2P3 (France); BMBF, DFG and MPG (Germany); INFN (Italy); NWO (The Netherlands); MNiSW and NCN (Poland); MEN/IFA (Romania); MSHE (Russia); MICINN (Spain); SNSF and SER (Switzerland); NASU (Ukraine); STFC (UK); DOE NP and NSF (USA). We acknowledge the computing resources that are provided by CERN, IN2P3 (France), KIT and DESY (Germany), INFN (Italy), SURF (The Netherlands), PIC (Spain), GridPP (UK), RRCKI and Yandex LLC (Russia), CSCS (Switzerland), IFIN-HH (Romania), CBPF (Brazil), PL-GRID (Poland) and NERSC (USA). We are indebted to the communities behind the multiple open-source software packages on which we depend. Individual groups or members have received support from ARC and ARDC (Australia); AvH Foundation (Germany); EPLANET, Marie Skłodowska-Curie Actions and ERC (European Union); A*MIDEX, ANR, IPhU and Labex P2IO, and Région Auvergne-Rhône-Alpes (France); Key Research Program

of Frontier Sciences of CAS, CAS PIFI, CAS CCEPP, Fundamental Research Funds for the Central Universities, and Sci. & Tech. Program of Guangzhou (China); RFBR, RSF and Yandex LLC (Russia); GVA, XuntaGal and GENCAT (Spain); the Leverhulme Trust, the Royal Society and UKRI (UK).

Data Availability Statement This manuscript has no associated data or the data will not be deposited. [Authors' comment: All LHCb scientific output is published in journals, with preliminary results made available in Conference Reports. All are Open Access, without restriction on use beyond the standard conditions agreed by CERN. Data associated to the plots in this publication are made available on the CERN document server at <http://cdsweb.cern.ch/record/2706539>.]

Open Access This article is licensed under a Creative Commons Attribution 4.0 International License, which permits use, sharing, adaptation, distribution and reproduction in any medium or format, as long as you give appropriate credit to the original author(s) and the source, provide a link to the Creative Commons licence, and indicate if changes were made. The images or other third party material in this article are included in the article's Creative Commons licence, unless indicated otherwise in a credit line to the material. If material is not included in the article's Creative Commons licence and your intended use is not permitted by statutory regulation or exceeds the permitted use, you will need to obtain permission directly from the copyright holder. To view a copy of this licence, visit <http://creativecommons.org/licenses/by/4.0/>.

Funded by SCOAP³.

References

1. S. Dimopoulos, S. Raby, F. Wilczek, Supersymmetry and the scale of unification. *Phys. Rev.* **D24**, 1681 (1981). <https://doi.org/10.1103/PhysRevD.24.1681>
2. S.P. Martin, A supersymmetry primer. *Adv. Ser. Direct. High Energy Phys.* **21**, 1 (2010). https://doi.org/10.1142/9789812839657_0001. [arXiv:hep-ph/9709356](https://arxiv.org/abs/hep-ph/9709356)
3. P.W. Graham, D.E. Kaplan, S. Rajendran, P. Saraswat, Displaced supersymmetry. *JHEP* **07**, 149 (2012). [https://doi.org/10.1007/JHEP07\(2012\)149](https://doi.org/10.1007/JHEP07(2012)149). [arXiv:1204.6038](https://arxiv.org/abs/1204.6038)
4. M.J. Strassler, K.M. Zurek, Discovering the Higgs through highly-displaced vertices. *Phys. Lett. B* **661**, 263 (2008). <https://doi.org/10.1016/j.physletb.2008.02.008>. [arXiv:hep-ph/0605193](https://arxiv.org/abs/hep-ph/0605193)
5. ATLAS Collaboration, G. Aad et al., Search for displaced vertices arising from decays of new heavy particles in 7 TeV pp collisions at ATLAS. *Phys. Lett. B* **707**, 478 (2012). <https://doi.org/10.1016/j.physletb.2011.12.057>. [arXiv:1109.2242](https://arxiv.org/abs/1109.2242)
6. ATLAS Collaboration, G. Aad et al., Search for massive, long-lived particles using multitrack displaced vertices or displaced lepton pairs in pp collisions at $\sqrt{s} = 8 \text{ TeV}$ with the ATLAS detector. *Phys. Rev. D* **92**, 072004 (2015). <https://doi.org/10.1103/PhysRevD.92.072004>. [arXiv:1504.05162](https://arxiv.org/abs/1504.05162)
7. CMS Collaboration, A.M. Sirunyan et al., Search for new long-lived particles at $\sqrt{s} = 13 \text{ TeV}$. *Phys. Lett. B* **780**, 432 (2018). <https://doi.org/10.1016/j.physletb.2018.03.019>. [arXiv:1711.09120](https://arxiv.org/abs/1711.09120)
8. ATLAS Collaboration, G. Aad et al., Search for long-lived, massive particles in events with a displaced vertex and a muon with large impact parameter in pp collisions at $\sqrt{s} = 13 \text{ TeV}$ with the atlas detector. *Phys. Rev. D* **102**, 032006 (2020). <https://doi.org/10.1103/physrevd.102.032006>. [arXiv:2003.11956](https://arxiv.org/abs/2003.11956)
9. LHCb Collaboration, R. Aaij et al., Search for massive long-lived particles decaying semileptonically in the LHCb detec-

- tor. Eur. Phys. J. C **77**, 224 (2017). <https://doi.org/10.1140/epjc/s10052-017-4744-6>. arXiv:1612.00945
10. P.W. Graham, S. Rajendran, P. Saraswat, Supersymmetric crevices: missing signatures of R-parity violation at the LHC. Phys. Rev. D **90**, 075005 (2014). <https://doi.org/10.1103/PhysRevD.90.075005>. arXiv:1403.7197
 11. L. Lee, C. Ohm, A. Soffer, T.-T. Yu, Collider searches for long-lived particles beyond the Standard Model. Prog. Part. Nucl. Phys. **106**, 210 (2019). <https://doi.org/10.1016/j.ppnp.2019.02.006>. arXiv:1810.12602
 12. J. Alimena et al., Searching for long-lived particles beyond the standard model at the large hadron collider. J. Phys. G Nucl. Part. Phys. **47**, 090501 (2020). <https://doi.org/10.1088/1361-6471/ab4574>. arXiv:1903.04497
 13. B.C. Allanach, A. Dedes, H.K. Dreiner, R parity violating minimal supergravity model. Phys. Rev. D **69**, 115002 (2004). <https://doi.org/10.1103/PhysRevD.69.115002>, <https://doi.org/10.1103/PhysRevD.72.079902>. arXiv:hep-ph/0309196
 14. LHCb Collaboration, A.A. Alves Jr. et al., The LHCb detector at the LHC. JINST **3**, S08005 (2008). <https://doi.org/10.1088/1748-0221/3/08/S08005>
 15. LHCb Collaboration, R. Aaij et al., LHCb detector performance. Int. J. Mod. Phys. A **30**, 1530022 (2015). <https://doi.org/10.1142/S0217751X15300227>. arXiv:1412.6352
 16. R. Aaij et al., Performance of the LHCb vertex locator. JINST **9**, P09007 (2014). <https://doi.org/10.1088/1748-0221/9/09/P09007>. arXiv:1405.7808
 17. R. Arink et al., Performance of the LHCb outer tracker. JINST **9**, P01002 (2014). <https://doi.org/10.1088/1748-0221/9/01/P01002>. arXiv:1311.3893
 18. P. d'Argent et al., Improved performance of the LHCb outer tracker in LHC Run 2. JINST **12**, P11016 (2017). <https://doi.org/10.1088/1748-0221/12/11/P11016>. arXiv:1708.00819
 19. M. Adinolfi et al., Performance of the LHCb RICH detector at the LHC. Eur. Phys. J. C **73**, 2431 (2013). <https://doi.org/10.1140/epjc/s10052-013-2431-9>. arXiv:1211.6759
 20. C. Abellán Beteta et al., Calibration and performance of the LHCb calorimeters in Run 1 and 2 at the LHC. Submitted to JINST. arXiv:2008.11556
 21. A.A. Alves Jr. et al., Performance of the LHCb muon system. JINST **8**, P02022 (2013). <https://doi.org/10.1088/1748-0221/8/02/P02022>. arXiv:1211.1346
 22. R. Aaij et al., The LHCb trigger and its performance in 2011. JINST **8**, P04022 (2013). <https://doi.org/10.1088/1748-0221/8/04/P04022>. arXiv:1211.3055
 23. R. Aaij et al., Performance of the LHCb trigger and full real-time reconstruction in Run 2 of the LHC. JINST **14**, P04013 (2019). <https://doi.org/10.1088/1748-0221/14/04/P04013>. arXiv:1812.10790
 24. T. Sjöstrand, S. Mrenna, P. Skands, A brief introduction to PYTHIA 8.1. Comput. Phys. Commun. **178**, 852 (2008). <https://doi.org/10.1016/j.cpc.2008.01.036>. arXiv:0710.3820
 25. T. Sjöstrand, S. Mrenna, P. Skands, PYTHIA 6.4 physics and manual. JHEP **05**, 026 (2006). <https://doi.org/10.1088/1126-6708/2006/05/026>. arXiv:hep-ph/0603175
 26. I. Belyaev et al., Handling of the generation of primary events in Gauss, the LHCb simulation framework. J. Phys. Conf. Ser. **331**, 032047 (2011). <https://doi.org/10.1088/1742-6596/331/3/032047>
 27. J. Pumplin et al., New generation of parton distributions with uncertainties from global QCD analysis. JHEP **07**, 012 (2002). <https://doi.org/10.1088/1126-6708/2002/07/012>. arXiv:hep-ph/0201195
 28. Geant4 Collaboration, J. Allison et al., Geant4 developments and applications. IEEE Trans. Nucl. Sci. **53**, 270 (2006). <https://doi.org/10.1109/TNS.2006.869826>
 29. Geant4 Collaboration, S. Agostinelli et al., Geant4: a simulation toolkit. Nucl. Instrum. Methods A **506**, 250 (2003). [https://doi.org/10.1016/S0168-9002\(03\)01368-8](https://doi.org/10.1016/S0168-9002(03)01368-8)
 30. M. Clemencic et al., The LHCb simulation application, Gauss: design, evolution and experience. J. Phys. Conf. Ser. **331**, 032023 (2011). <https://doi.org/10.1088/1742-6596/331/3/032023>
 31. M. Kucharczyk, P. Morawski, M. Witek, Primary vertex reconstruction at LHCb. CERN-LHCb-PUB-2014-044, LHCb-PUB-2014-044 (2014)
 32. LHCb Collaboration, R. Aaij et al., Search for the rare decay, $K_S^0 \rightarrow \mu^+ \mu^-$. JHEP **01**, 090 (2013). [https://doi.org/10.1007/JHEP01\(2013\)090](https://doi.org/10.1007/JHEP01(2013)090). arXiv:1209.4029
 33. LHCb Collaboration, R. Aaij et al., Measurement of the b-quark production cross-section in 7 and 13 TeV pp collisions. Phys. Rev. Lett. **118**, 052002 (2017). <https://doi.org/10.1103/PhysRevLett.118.052002>. arXiv:1612.05140 [Erratum ibid. **119**, 169901 (2017)]. <https://doi.org/10.1103/PhysRevLett.119.169901>
 34. A. Pearce, LHCb early Run 2 measurements of B and charm production, LHCb-PROC-2016-001
 35. J. Alwall et al., The automated computation of tree-level and next-to-leading order differential cross sections, and their matching to parton shower simulations. J. High Energ. Phys. **2014**, 79 (2014). [https://doi.org/10.1007/jhep07\(2014\)079](https://doi.org/10.1007/jhep07(2014)079). arXiv:1405.0301
 36. L. Breiman, J.H. Friedman, R.A. Olshen, C.J. Stone, *Classification and Regression Trees* (Wadsworth International Group, Belmont, 1984)
 37. Y. Freund, R.E. Schapire, A decision-theoretic generalization of on-line learning and an application to boosting. J. Comput. Syst. Sci. **55**, 119 (1997). <https://doi.org/10.1006/jcss.1997.1504>
 38. M. Botje et al., The PDF4LHC working group interim recommendations. arXiv:1101.0538
 39. J. Butterworth et al., PDF4LHC recommendations for LHC Run II. J. Phys. **G43**, 023001 (2016). <https://doi.org/10.1088/0954-3899/43/2/023001>. arXiv:1510.03865
 40. LHCb Collaboration, R. Aaij et al., Precision luminosity measurements at LHCb. JINST **9**, P12005 (2014). <https://doi.org/10.1088/1748-0221/9/12/P12005>. arXiv:1410.0149
 41. LHCb Collaboration, R. Aaij et al., Measurements of the B^+ , B^0 , B_s^0 meson and Λ_b^0 baryon lifetimes. JHEP **04**, 114 (2014). [https://doi.org/10.1007/JHEP04\(2014\)114](https://doi.org/10.1007/JHEP04(2014)114). arXiv:1402.2554
 42. A.L. Read, Presentation of search results: the CL_s technique. J. Phys. **G28**, 2693 (2002). <https://doi.org/10.1088/0954-3899/28/10/313>
 43. ATLAS Collaboration, G. Aad et al., Combined measurements of Higgs boson production and decay using up to 80 fb^{-1} of proton-proton collision data at $\sqrt{s} = 13 \text{ TeV}$ collected with the ATLAS experiment. Phys. Rev. D **101**, 012002 (2020). <https://doi.org/10.1103/PhysRevD.101.012002>. arXiv:1909.02845

LHCb Collaboration

R. Aaij³², A. S. W. Abdelmotteleb⁵⁶, C. Abellán Beteta⁵⁰, F. J. Abudinen Gallego⁵⁶, T. Ackernley⁶⁰, B. Adeva⁴⁶, M. Adinolfi⁵⁴, H. Afsharnia⁹, C. Agapopoulou¹³, C. A. Aidala⁸⁷, S. Aiola²⁵, Z. Ajaltouni⁹, S. Akar⁶⁵, J. Albrecht¹⁵, F. Alessio⁴⁸, M. Alexander⁵⁹, A. Alfonso Albero⁴⁵, Z. Aliouche⁶², G. Alkhazov³⁸, P. Alvarez Cartelle⁵⁵, S. Amato², J. L. Amey⁵⁴, Y. Amhis¹¹, L. An⁴⁸, L. Anderlini²², A. Andreianov³⁸, M. Andreotti²¹, F. Archilli¹⁷, A. Artamonov⁴⁴, M. Artuso⁶⁸, K. Arzymatov⁴², E. Aslanides¹⁰, M. Atzeni⁵⁰, B. Audurier¹², S. Bachmann¹⁷, M. Bachmayer⁴⁹, J. J. Back⁵⁶, P. Baladron Rodriguez⁴⁶, V. Balagura¹², W. Baldini²¹, J. Baptista Leite¹, M. Barbetti²², R. J. Barlow⁶², S. Barsuk¹¹, W. Barter⁶¹, M. Bartolini^{24,h}, F. Baryshnikov⁸³, J. M. Basels¹⁴, S. Bashir³⁴, G. Bassi²⁹, B. Batsukh⁶⁸, A. Battig¹⁵, A. Bay^{49,a}, A. Beck⁵⁶, M. Becker¹⁵, F. Bedeschi²⁹, I. Bediaga¹, A. Beiter⁶⁸, V. Belavin⁴², S. Belin²⁷, V. Bellei⁵⁰, K. Belous⁴⁴, I. Belov⁴⁰, I. Belyaev⁴¹, G. Bencivenni²³, E. Ben-Haim¹³, A. Berezhnoy⁴⁰, R. Bernet⁵⁰, D. Berninghoff¹⁷, H. C. Bernstein⁶⁸, C. Bertella⁴⁸, A. Bertolin²⁸, C. Betancourt⁵⁰, F. Betti⁴⁸, Ia. Bezshyiko⁵⁰, S. Bhasin⁵⁴, J. Bhom³⁵, L. Bian⁷³, M. S. Bieker¹⁵, S. Bifani⁵³, P. Billoir¹³, M. Birch⁶¹, F. C. R. Bishop⁵⁵, A. Bitadze⁶², A. Bizzeti^{22,k}, M. Bjørn⁶³, M. P. Blago⁴⁸, T. Blake⁵⁶, F. Blanc⁴⁹, S. Blusk⁶⁸, D. Bobulska⁵⁹, J. A. Boelhauve¹⁵, O. Boente Garcia⁴⁶, T. Boettcher⁶⁵, A. Boldyrev⁸², A. Bondar⁴³, N. Bondar^{38,48}, S. Borghi⁶², M. Borisjak⁴², M. Borsato¹⁷, J. T. Borsuk³⁵, S. A. Bouchiba⁴⁹, T. J. V. Bowcock⁶⁰, A. Boyer⁴⁸, C. Bozzi²¹, M. J. Bradley⁶¹, S. Braun⁶⁶, A. Brea Rodriguez⁴⁶, M. Brodski⁴⁸, J. Brodzicka³⁵, A. Brossa Gonzalo⁵⁶, D. Brundu²⁷, A. Buonaura⁵⁰, L. Buonincontri²⁸, A. T. Burke⁶², C. Burr⁴⁸, A. Bursche⁷², A. Butkevich³⁹, J. S. Butter³², J. Buytaert⁴⁸, W. Byczynski⁴⁸, S. Cadeddu²⁷, H. Cai⁷³, R. Calabrese^{21,f}, L. Calefice^{13,15}, L. Calero Diaz²³, S. Cali²³, R. Calladine⁵³, M. Calvi^{26,j}, M. Calvo Gomez⁸⁵, P. Camargo Magalhaes⁵⁴, P. Campana²³, A. F. Campoverde Quezada⁶, S. Capelli^{26,j}, L. Capriotti^{20,d}, A. Carbone^{20,d}, G. Carboni³¹, R. Cardinale^{24,h}, A. Cardini²⁷, I. Carli⁴, P. Carniti^{26,j}, L. Carus¹⁴, K. Carvalho Akiba³², A. Casais Vidal⁴⁶, G. Casse⁶⁰, M. Cattaneo⁴⁸, G. Cavallero⁴⁸, S. Celani⁴⁹, J. Cerasoli¹⁰, D. Cervenkov⁶³, A. J. Chadwick⁶⁰, M. G. Chapman⁵⁴, M. Charles¹³, Ph. Charpentier⁴⁸, G. Chatzikostantinidis⁵³, C. A. Chavez Barajas⁶⁰, M. Chefdeville⁸, C. Chen³, S. Chen⁴, A. Chernov³⁵, V. Chobanova⁴⁶, S. Cholak⁴⁹, M. Chrzaszcz³⁵, A. Chubykin³⁸, V. Chulikov³⁸, P. Ciambrone²³, M. F. Cicala⁵⁶, X. Cid Vidal⁴⁶, G. Ciezarek⁴⁸, P. E. L. Clarke⁵⁸, M. Clemencic⁴⁸, H. V. Cliff⁵⁵, J. Closier⁴⁸, J. L. Cobbley⁶², V. Coco⁴⁸, J. A. B. Coelho¹¹, J. Cogan¹⁰, E. Cogneras⁹, L. Cojocariu³⁷, P. Collins⁴⁸, T. Colombo⁴⁸, L. Congedo^{19,c}, A. Contu²⁷, N. Cooke⁵³, G. Coombs⁵⁹, I. Corredoira⁴⁶, G. Corti⁴⁸, C. M. Costa Sobral⁵⁶, B. Couturier⁴⁸, D. C. Craik⁶⁴, J. Crkovská⁶⁷, M. Cruz Torres¹, R. Currie⁵⁸, C. L. Da Silva⁶⁷, S. Dadabaev⁸³, L. Dai⁷¹, E. Dall'Occo¹⁵, J. Dalseno⁴⁶, C. D'Ambrosio⁴⁸, A. Danilina⁴¹, P. d'Argent⁴⁸, J. E. Davies⁶², A. Davis⁶², O. De Aguiar Francisco⁶², K. De Bruyn⁷⁹, S. De Capua⁶², M. De Cian⁴⁹, J. M. De Miranda¹, L. De Paula², M. De Serio^{19,c}, D. De Simone⁵⁰, P. De Simone²³, J. A. de Vries⁸⁰, C. T. Dean⁶⁷, D. Decamp⁸, V. Dedu¹⁰, L. Del Buono¹³, B. Delaney⁵⁵, H.-P. Dembinski¹⁵, A. Dendek³⁴, V. Denysenko⁵⁰, D. Derkach⁸², O. Deschamps⁹, F. Desse¹¹, F. Dettori^{27,e}, B. Dey⁷⁷, A. Di Cicco²³, P. Di Nezza²³, S. Didenko⁸³, L. Dieste Maronas⁴⁶, H. Dijkstra⁴⁸, V. Dobishuk⁵², C. Dong³, A. M. Donohoe¹⁸, F. Dordei²⁷, A. C. dos Reis¹, L. Douglas⁵⁹, A. Dovbnya⁵¹, A. G. Downes⁸, M. W. Dudek³⁵, L. Dufour⁴⁸, V. Duk⁷⁸, P. Durante⁴⁸, J. M. Durham⁶⁷, D. Dutta⁶², A. Dziurda³⁵, A. Dzyuba³⁸, S. Easo⁵⁷, U. Egede⁶⁹, V. Egorychev⁴¹, S. Eidelman^{43,v}, S. Eisenhardt⁵⁸, S. Ek-In⁴⁹, L. Eklund^{59,86}, S. Ely⁶⁸, A. Ene³⁷, E. Epple⁶⁷, S. Escher¹⁴, J. Eschle⁵⁰, S. Esen¹³, T. Evans⁴⁸, A. Falabella²⁰, J. Fan³, Y. Fan⁶, B. Fang⁷³, S. Farry⁶⁰, D. Fazzini^{26,j}, M. Féo⁴⁸, A. Fernandez Prieto⁴⁶, J. M. Fernandez-tenllado Arribas⁴⁵, A. D. Fernez⁶⁶, F. Ferrari^{20,d}, L. Ferreira Lopes⁴⁹, F. Ferreira Rodrigues², S. Ferreres Sole³², M. Ferrillo⁵⁰, M. Ferro-Luzzi⁴⁸, S. Filippov³⁹, R. A. Fini¹⁹, M. Fiorini^{21,f}, M. Firlej³⁴, K. M. Fischer⁶³, D. S. Fitzgerald⁸⁷, C. Fitzpatrick⁶², T. Fiutowski³⁴, A. Fkiaras⁴⁸, F. Fleuret¹², M. Fontana¹³, F. Fontanelli^{24,h}, R. Forty⁴⁸, D. Foulds-Holt⁵⁵, V. Franco Lima⁶⁰, M. Franco Sevilla⁶⁶, M. Frank⁴⁸, E. Franzoso²¹, G. Frau¹⁷, C. Frei⁴⁸, D. A. Friday⁵⁹, J. Fu⁶, Q. Fuehring¹⁵, E. Gabriel³², G. Galati^{19,c}, A. Gallas Torreira⁴⁶, D. Galli^{20,d}, S. Gambetta^{48,58}, Y. Gan³, M. Gandelman², P. Gandini²⁵, Y. Gao⁵, M. Garau²⁷, L. M. Garcia Martin⁵⁶, P. Garcia Moreno⁴⁵, J. García Pardiñas^{26,j}, B. Garcia Plana⁴⁶, F. A. Garcia Rosales¹², L. Garrido⁴⁵, C. Gaspar⁴⁸, R. E. Geertsema³², D. Gerick¹⁷, L. L. Gerken¹⁵, E. Gersabeck⁶², M. Gersabeck⁶², T. Gershon⁵⁶, D. Gerstel¹⁰, Ph. Ghez⁸, L. Giambastiani²⁸, V. Gibson⁵⁵, H. K. Giemza³⁶, A. L. Gilman⁶³, M. Giovannetti^{23,p}, A. Gioventù⁴⁶, P. Gironella Gironell⁴⁵, L. Giubega³⁷, C. Giugliano^{21,f,48}, K. Gisdov⁵⁸, E. L. Gkougkousis⁴⁸, V. V. Gligorov¹³, C. Göbel⁷⁰, E. Golobardes⁸⁵, D. Golubkov⁴¹, A. Golutvin^{61,83}, A. Gomes^{1,a}, S. Gomez Fernandez⁴⁵, F. Goncalves Abrantes⁶³, M. Goncerz³⁵, G. Gong³, P. Gorbounov⁴¹, I. V. Gorelov⁴⁰, C. Gotti²⁶, E. Govorkova⁴⁸, J. P. Grabowski¹⁷, T. Grammatico¹³, L. A. Granado Cardoso⁴⁸, E. Graugés⁴⁵, E. Graverini⁴⁹, G. Graziani²², A. Grecu³⁷, L. M. Greeven³², N. A. Grieser⁴, L. Grillo⁶², S. Gromov⁸³, B. R. Gruberg Cazon⁶³, C. Gu³, M. Guarise²¹, M. Guittiere¹¹, P. A. Günther¹⁷, E. Gushchin³⁹, A. Guth¹⁴, Y. Guz⁴⁴, T. Gys⁴⁸, T. Hadavizadeh⁶⁹, G. Haefeli⁴⁹, C. Haen⁴⁸, J. Haimberger⁴⁸, T. Halewood-leagas⁶⁰, P. M. Hamilton⁶⁶, J. P. Hammerich⁶⁰, Q. Han⁷, X. Han¹⁷, T. H. Hancock⁶³, S. Hansmann-Menzemer¹⁷, N. Harnew⁶³, T. Harrison⁶⁰, C. Hasse⁴⁸, M. Hatch⁴⁸, J. He^{6,b},

- M. Hecker⁶¹, K. Heijhoff³², K. Heinicke¹⁵, A. M. Hennequin⁴⁸, K. Hennessy⁶⁰, L. Henry⁴⁸, J. Heuel¹⁴, A. Hicheur², D. Hill⁴⁹, M. Hilton⁶², S. E. Hollitt¹⁵, R. Hou⁷, Y. Hou⁶, J. Hu¹⁷, J. Hu⁷², W. Hu⁷, X. Hu³, W. Huang⁶, X. Huang⁷³, W. Hulsbergen³², R. J. Hunter⁵⁶, M. Hushchyn⁸², D. Hutchcroft⁶⁰, D. Hynds³², P. Ibis¹⁵, M. Idzik³⁴, D. Ilin³⁸, P. Ilten⁶⁵, A. Inglessi³⁸, A. Ishteev⁸³, K. Ivshin³⁸, R. Jacobsson⁴⁸, H. Jage¹⁴, S. Jakobsen⁴⁸, E. Jans³², B. K. Jashai⁴⁷, A. Jawahery⁶⁶, V. Jevtic¹⁵, F. Jiang³, M. John⁶³, D. Johnson⁴⁸, C. R. Jones⁵⁵, T. P. Jones⁵⁶, B. Jost⁴⁸, N. Jurik⁴⁸, S. H. Kalavan Kadavath³⁴, S. Kandybei⁵¹, Y. Kang³, M. Karacson⁴⁸, M. Karpov⁸², F. Keizer⁴⁸, D. M. Keller⁶⁸, M. Kenzie⁵⁶, T. Ketel³³, B. Khanji¹⁵, A. Kharisova⁸⁴, S. Khodenko⁴⁴, T. Kirn¹⁴, V. S. Kirsebom⁴⁹, O. Kitouni⁶⁴, S. Klaver³², N. Kleijne²⁹, K. Klimaszewski³⁶, M. R. Kmiec³⁶, S. Koliiev⁵², A. Kondybaya⁸³, A. Konoplyannikov⁴¹, P. Kopciewicz³⁴, R. Kopecna¹⁷, P. Koppenburg³², M. Korolev⁴⁰, I. Kostiuk^{32,52}, O. Kot⁵², S. Kotriakhova^{21,38}, P. Kravchenko³⁸, L. Kravchuk³⁹, R. D. Krawczyk⁴⁸, M. Kreps⁵⁶, F. Kress⁶¹, S. Kretzschmar¹⁴, P. Krokovny^{43,v}, W. Krupa³⁴, W. Krzemien³⁶, M. Kucharczyk³⁵, V. Kudryavtsev^{43,v}, H. S. Kuindersma^{32,33}, G. J. Kunde⁶⁷, T. Kvaratskheliya⁴¹, D. Lacarrere⁴⁸, G. Lafferty⁶², A. Lal²⁷, A. Lampis²⁷, D. Lancierini⁵⁰, J. J. Lane⁶², R. Lane⁵⁴, G. Lanfranchi²³, C. Langenbruch¹⁴, J. Langer¹⁵, O. Lantwin⁸³, T. Latham⁵⁶, F. Lazzari^{29,q}, R. Le Gac¹⁰, S. H. Lee⁸⁷, R. Lefèvre⁹, A. Leflat⁴⁰, S. Legotin⁸³, O. Leroy¹⁰, T. Lesiak³⁵, B. Leverington¹⁷, H. Li⁷², P. Li¹⁷, S. Li⁷, Y. Li⁴, Y. Li⁴, Z. Li⁶⁸, X. Liang⁶⁸, T. Lin⁶¹, R. Lindner⁴⁸, V. Lisovskyi¹⁵, R. Litvinov²⁷, G. Liu⁷², H. Liu⁶, Q. Liu⁶, S. Liu⁴, A. Lobo Salvia⁴⁵, A. Loi²⁷, J. Lomba Castro⁴⁶, I. Longstaff⁵⁹, J. H. Lopes², S. Lopez Solino⁴⁶, G. H. Lovell⁵⁵, Y. Lu⁴, C. Lucarelli²², D. Lucchesi^{28,1}, S. Luchuk³⁹, M. Lucio Martinez³², V. Lukashenko^{32,52}, Y. Luo³, A. Lupato⁶², E. Luppi^{21,f}, O. Lupton⁵⁶, A. Lusiani^{29,m}, X. Lyu⁶, L. Ma⁴, R. Ma⁶, S. Maccolini^{20,d}, F. Machefert¹¹, F. Maciuc³⁷, V. Macko⁴⁹, P. Mackowiak¹⁵, S. Maddrell-Mander⁵⁴, O. Madejczyk^t, L. R. Madhan Mohan⁵⁴, O. Maevskiy⁸², A. Maevskiy⁸², D. Maisuzenko³⁸, M. W. Majewski^t, J. J. Malczewski³⁵, S. Malde⁶³, B. Malecki⁴⁸, A. Malinin⁸¹, T. Maltsev^{43,v}, H. Malygina¹⁷, G. Manca^{27,e}, G. Mancinelli¹⁰, D. Manuzzi^{20,d}, D. Marangotto^{25,i}, J. Maratas^{9,s}, J. F. Marchand⁸, U. Marconi²⁰, S. Mariani^{22,g}, C. Marin Benito⁴⁸, M. Marinangeli⁴⁹, J. Marks¹⁷, A. M. Marshall⁵⁴, P. J. Marshall⁶⁰, G. Martelli⁷⁸, G. Martellotti³⁰, L. Martinazzoli^{48,j}, M. Martinelli^{26,j}, D. Martinez Santos⁴⁶, F. Martinez Vidal⁴⁷, A. Massafferri¹, M. Materok¹⁴, R. Matev⁴⁸, A. Mathad⁵⁰, Z. Mathe⁴⁸, V. Matiunin⁴¹, C. Matteuzzi²⁶, K. R. Mattioli⁸⁷, A. Mauri³², E. Maurice¹², J. Mauricio⁴⁵, M. Mazurek⁴⁸, M. McCann⁶¹, L. McConnell¹⁸, T. H. McGrath⁶², N. T. McHugh⁵⁹, A. McNab⁶², R. McNulty¹⁸, J. V. Mead⁶⁰, B. Meadows⁶⁵, G. Meier¹⁵, N. Meinert⁷⁶, D. Melnychuk³⁶, S. Meloni^{26,j}, M. Merk^{32,80}, A. Merli²⁵, L. Meyer Garcia², M. Mikhasenko⁴⁸, D. A. Milanes⁷⁴, E. Millard⁵⁶, M. Milovanovic⁴⁸, M.-N. Minard⁸, A. Minotti^{26,j}, L. Minzoni^{21,f}, S. E. Mitchell⁵⁸, B. Mitreska⁶², D. S. Mitzel⁴⁸, A. Mödden¹⁵, R. A. Mohammed⁶³, R. D. Moise⁶¹, S. Mokhnenko⁸², T. Mombächer⁴⁶, I. A. Monroy⁷⁴, S. Monteil⁹, M. Morandin²⁸, G. Morello²³, M. J. Morello^{29,m}, J. Moron³⁴, A. B. Morris⁷⁵, A. G. Morris⁵⁶, R. Mountain⁶⁸, H. Mu³, F. Muheim^{48,58}, M. Mulder⁴⁸, D. Müller⁴⁸, K. Müller⁵⁰, C. H. Murphy⁶³, D. Murray⁶², P. Muzzetto^{27,48}, P. Naik⁵⁴, T. Nakada⁴⁹, R. Nandakumar⁵⁷, T. Nanut⁴⁹, I. Nasteva², M. Needham⁵⁸, I. Neri²¹, N. Neri^{25,i}, S. Neubert⁷⁵, N. Neufeld⁴⁸, R. Newcombe⁶¹, T. D. Nguyen⁴⁹, C. Nguyen-Mau^{49,w}, E. M. Niel¹¹, S. Nieswand¹⁴, N. Nikitin⁴⁰, N. S. Nolte⁶⁴, C. Normand⁸, C. Nunez⁸⁷, A. Oblakowska-Mucha³⁴, V. Obraztsov⁴⁴, T. Oeser¹⁴, D. P. O'Hanlon⁵⁴, S. Okamura²¹, R. Oldeman^{27,e}, F. Oliva⁵⁸, M. E. Olivares⁶⁸, C. J. G. Onderwater⁷⁹, R. H. O'Neil⁵⁸, J. M. Otalora Goicochea², T. Ovsianikova⁴¹, P. Owen⁵⁰, A. Oyanguren⁴⁷, K. O. Padéken⁷⁵, B. Pagare⁵⁶, P. R. Pais⁴⁸, T. Pajero⁶³, A. Palano¹⁹, M. Palutan²³, Y. Pan⁶², G. Panshin⁸⁴, A. Papanestis⁵⁷, M. Pappagallo^{19,c}, L. L. Pappalardo^{21,f}, C. Pappenheimer⁶⁵, W. Parker⁶⁶, C. Parkes⁶², B. Passalacqua²¹, G. Passaleva²², A. Pastore¹⁹, M. Patel⁶¹, C. Patrignani^{20,d}, C. J. Pawley⁸⁰, A. Pearce⁴⁸, A. Pellegrino³², M. Pepe Altarelli⁴⁸, S. Perazzini²⁰, D. Pereima⁴¹, A. Pereiro Castro⁴⁶, P. Perret⁹, M. Petric^{48,59}, K. Petridis⁵⁴, A. Petrolini^{24,h}, A. Petrov⁸¹, S. Petrucci⁵⁸, M. Petruzzo²⁵, T. T. H. Pham⁶⁸, L. Pica^{29,m}, M. Piccini⁷⁸, B. Pietrzyl⁸, G. Pietrzyl⁴⁹, M. Pili⁶³, D. Pinci³⁰, F. Pisani⁴⁸, M. Pizzichemi⁴⁸, P. K. Resmi¹⁰, V. Placinta³⁷, J. Plews⁵³, M. Plo Casasus⁴⁶, F. Polci¹³, M. Poli Lener²³, M. Poliakova⁶⁸, A. Poluektov¹⁰, N. Polukhina^{83,u}, I. Polyakov⁶⁸, E. Polycarpo², S. Ponce⁴⁸, D. Popov^{6,48}, S. Popov⁴², S. Poslavskii⁴⁴, K. Prasanth³⁵, L. Promberger⁴⁸, C. Prouve⁴⁶, V. Pugatch⁵², V. Puill¹¹, H. Pullen⁶³, G. Punzi^{29,n}, H. Qi³, W. Qian⁶, J. Qin⁶, N. Qin³, R. Quagliani⁴⁹, B. Quintana⁸, N. V. Raab¹⁸, R. I. Rabadan Trejo⁶, B. Rachwal³⁴, J. H. Rademacker⁵⁴, M. Rama²⁹, M. Ramos Pernas⁵⁶, M. S. Rangel², F. Ratnikov^{42,82}, G. Raven³³, M. Reboud⁸, F. Redi⁴⁹, F. Reiss⁶², C. Remon Alepuz⁴⁷, Z. Ren³, V. Renaudin⁶³, R. Ribatti²⁹, S. Ricciardi⁵⁷, K. Rinnert⁶⁰, P. Robbe¹¹, G. Robertson⁵⁸, A. B. Rodrigues⁴⁹, E. Rodrigues⁶⁰, J. A. Rodriguez Lopez⁷⁴, E. R. R. Rodriguez Rodriguez⁴⁶, A. Rollings⁶³, P. Roloff⁴⁸, V. Romanovskiy⁴⁴, M. Romero Lamas⁴⁶, A. Romero Vidal⁴⁶, J. D. Roth⁸⁷, M. Rotondo²³, M. S. Rudolph⁶⁸, T. Ruf⁴⁸, R. A. Ruiz Fernandez⁴⁶, J. Ruiz Vidal⁴⁷, A. Ryzhikov⁸², J. Ryzka³⁴, J. J. Saborido Silva⁴⁶, N. Sagidova³⁸, N. Sahoo⁵⁶, B. Saitta^{27,e}, M. Salomoni⁴⁸, D. Sanchez Gonzalo⁴⁵, C. Sanchez Gras³², R. Santacesaria³⁰, C. Santamarina Rios⁴⁶, M. Santimaria²³, E. Santovetti^{31,p}, D. Saranin⁸³, G. Sarpis¹⁴, M. Sarpis⁷⁵, A. Sarti³⁰, C. Satriano^{30,o}, A. Satta³¹, M. Saur¹⁵, D. Savrina^{40,41}, H. Sazak⁹, L. G. Scantlebury Smead⁶³, A. Scarabotto¹³, S. Schael¹⁴, S. Scherl⁶⁰, M. Schiller⁵⁹, H. Schindler⁴⁸, M. Schmelling¹⁶, B. Schmidt⁴⁸, S. Schmitt¹⁴, O. Schneider⁴⁹, A. Schopper⁴⁸, M. Schubiger³²,

S. Schulte⁴⁹, M. H. Schune¹¹, R. Schwemmer⁴⁸, B. Sciascia^{23,48}, S. Sellam⁴⁶, A. Semennikov⁴¹, M. Senghi Soares³³, A. Sergi^{24,h}, N. Serra⁵⁰, L. Sestini²⁸, A. Seuthe¹⁵, Y. Shang⁵, D. M. Shangase⁸⁷, M. Shapkin⁴⁴, I. Shchemberov⁸³, L. Shchutska⁴⁹, T. Shears⁶⁰, L. Shekhtman^{43,v}, Z. Shen⁵, V. Shevchenko⁸¹, E. B. Shields^{26,j}, Y. Shimizu¹¹, E. Shmanin⁸³, J. D. Shupperd⁶⁸, B. G. Siddi²¹, R. Silva Coutinho⁵⁰, G. Simi²⁸, S. Simone^{19,c}, N. Skidmore⁶², T. Skwarnicki⁶⁸, M. W. Slater⁵³, I. Slazyk^{21,f}, J. C. Smallwood⁶³, J. G. Smeaton⁵⁵, A. Smetkina⁴¹, E. Smith⁵⁰, M. Smith⁶¹, A. Snoch³², M. Soares²⁰, L. Soares Lavra⁹, M. D. Sokoloff⁶⁵, F. J. P. Soler⁵⁹, A. Solovev³⁸, I. Solov'yev³⁸, F. L. Souza De Almeida², B. Souza De Paula², B. Spaan¹⁵, E. Spadaro Norella²⁵, P. Spradlin⁵⁹, F. Stagni⁴⁸, M. Stahl⁶⁵, S. Stahl⁴⁸, S. Stanislaus⁶³, O. Steinkamp^{50,83}, O. Stenyakin⁴⁴, H. Stevens¹⁵, S. Stone⁶⁸, M. Straticiuc³⁷, D. Strekalina⁸³, F. Suljik⁶³, J. Sun²⁷, L. Sun⁷³, Y. Sun⁶⁶, P. Svihra⁶², P. N. Swallow⁵³, K. Swientek³⁴, A. Szabelski³⁶, T. Szumlak³⁴, M. Szymanski⁴⁸, S. Taneja⁶², A. R. Tanner⁵⁴, M. D. Tat⁶³, A. Terentev⁸³, F. Teubert⁴⁸, E. Thomas⁴⁸, D. J. D. Thompson⁵³, K. A. Thomson⁶⁰, V. Tisserand⁹, S. T'Jampens⁸, M. Tobin⁴, L. Tomassetti^{21,f}, X. Tong⁵, D. Torres Machado¹, D. Y. Tou¹³, M. T. Tran⁴⁹, E. Trifonova⁸³, C. Trippi⁴⁹, G. Tuci⁶, A. Tully⁴⁹, N. Tuning^{32,48}, A. Ukleja³⁶, D. J. Unverzagt¹⁷, E. Ursov⁸³, A. Usachov³², A. Ustyuzhanin^{42,82}, U. Uwer¹⁷, A. Vagner⁸⁴, V. Vagnoni²⁰, A. Valassi⁴⁸, G. Valenti²⁰, N. Valls Canudas⁸⁵, M. van Beuzekom³², M. Van Dijk⁴⁹, E. van Herwijnen⁸³, C. B. Van Hulse¹⁸, M. van Veghel⁷⁹, R. Vazquez Gomez⁴⁶, P. Vazquez Regueiro⁴⁶, C. Vázquez Sierra⁴⁸, S. Vecchi²¹, J. J. Velthuis⁵⁴, M. Veltri^{22,r}, A. Venkateswaran⁶⁸, M. Veronesi³², M. Vesterinen⁵⁶, D. Vieira⁶⁵, M. Vieites Diaz⁴⁹, H. Viemann⁷⁶, X. Vilasis-Cardona⁸⁵, E. Vilella Figueras⁶⁰, A. Villa²⁰, P. Vincent¹³, F. C. Volle¹¹, D. Vom Bruch¹⁰, A. Vorobyev³⁸, V. Vorobyev^{43,v}, N. Voropaev³⁸, K. Vos⁸⁰, R. Waldi¹⁷, J. Walsh²⁹, C. Wang¹⁷, J. Wang⁵, J. Wang⁴, J. Wang³, J. Wang⁷³, M. Wang³, R. Wang⁵⁴, Y. Wang⁷, Z. Wang⁵⁰, Z. Wang³, Z. Wang⁶, J. A. Ward⁵⁶, N. K. Watson⁵³, S. G. Weber¹³, D. Websdale⁶¹, C. Weisser⁶⁴, B. D. C. Westhenry⁵⁴, D. J. White⁶², M. Whitehead⁵⁴, A. R. Wiederhold⁵⁶, D. Wiedner¹⁵, G. Wilkinson⁶³, M. Wilkinson⁶⁸, I. Williams⁵⁵, M. Williams⁶⁴, M. R. J. Williams⁵⁸, F. F. Wilson⁵⁷, W. Wislicki³⁶, M. Witek³⁵, L. Witola¹⁷, G. Wormser¹¹, S. A. Wotton⁵⁵, H. Wu⁶⁸, K. Wyllie⁴⁸, Z. Xiang⁶, D. Xiao⁷, Y. Xie⁷, A. Xu⁵, J. Xu⁶, L. Xu³, M. Xu⁷, Q. Xu⁶, Z. Xu⁵, Z. Xu⁶, D. Yang³, S. Yang⁶, Y. Yang⁶, Z. Yang⁵, Z. Yang⁶⁶, Y. Yao⁶⁸, L. E. Yeomans⁶⁰, H. Yin⁷, J. Yu⁷¹, X. Yuan⁶⁸, O. Yushchenko⁴⁴, E. Zaffaroni⁴⁹, M. Zavertyaev^{16,u}, M. Zdybal³⁵, O. Zenaiev⁴⁸, M. Zeng³, D. Zhang⁷, L. Zhang³, S. Zhang⁷¹, S. Zhang⁵, Y. Zhang⁵, Y. Zhang⁶³, A. Zharkova⁸³, A. Zhelezov¹⁷, Y. Zheng⁶, T. Zhou⁵, X. Zhou⁶, Y. Zhou⁶, V. Zhovkovska¹¹, X. Zhu³, X. Zhu⁷, Z. Zhu⁶, V. Zhukov^{14,40}, J. B. Zonneveld⁵⁸, Q. Zou⁴, S. Zucchelli^{20,d}, D. Zuliani²⁸, G. Zunică⁶²

¹ Centro Brasileiro de Pesquisas Físicas (CBPF), Rio de Janeiro, Brazil² Universidade Federal do Rio de Janeiro (UFRJ), Rio de Janeiro, Brazil³ Center for High Energy Physics, Tsinghua University, Beijing, China⁴ Institute of High Energy Physics (IHEP), Beijing, China⁵ School of Physics State Key Laboratory of Nuclear Physics and Technology, Peking University, Beijing, China⁶ University of Chinese Academy of Sciences, Beijing, China⁷ Institute of Particle Physics, Central China Normal University, Wuhan, Hubei, China⁸ Univ. Savoie Mont Blanc, CNRS, IN2P3-LAPP, Annecy, France⁹ Université Clermont Auvergne, CNRS/IN2P3, LPC, Clermont-Ferrand, France¹⁰ Aix Marseille Univ, CNRS/IN2P3, CPPM, Marseille, France¹¹ Université Paris-Saclay, CNRS/IN2P3, IJCLab, Orsay, France¹² Laboratoire Leprince-Ringuet, CNRS/IN2P3, Ecole Polytechnique, Institut Polytechnique de Paris, Palaiseau, France¹³ LPNHE, Sorbonne Université, Paris Diderot Sorbonne Paris Cité, CNRS/IN2P3, Paris, France¹⁴ I. Physikalisches Institut, RWTH Aachen University, Aachen, Germany¹⁵ Fakultät Physik, Technische Universität Dortmund, Dortmund, Germany¹⁶ Max-Planck-Institut für Kernphysik (MPIK), Heidelberg, Germany¹⁷ Physikalisches Institut, Ruprecht-Karls-Universität Heidelberg, Heidelberg, Germany¹⁸ School of Physics, University College Dublin, Dublin, Ireland¹⁹ INFN Sezione di Bari, Bari, Italy²⁰ INFN Sezione di Bologna, Bologna, Italy²¹ INFN Sezione di Ferrara, Ferrara, Italy²² INFN Sezione di Firenze, Florence, Italy²³ INFN Laboratori Nazionali di Frascati, Frascati, Italy²⁴ INFN Sezione di Genova, Genoa, Italy²⁵ INFN Sezione di Milano, Milan, Italy²⁶ INFN Sezione di Milano-Bicocca, Milan, Italy

- ²⁷ INFN Sezione di Cagliari, Monserrato, Italy
²⁸ Universita degli Studi di Padova, Universita e INFN, Padova, Padua, Italy
²⁹ INFN Sezione di Pisa, Pisa, Italy
³⁰ INFN Sezione di Roma La Sapienza, Rome, Italy
³¹ INFN Sezione di Roma Tor Vergata, Rome, Italy
³² Nikhef National Institute for Subatomic Physics, Amsterdam, The Netherlands
³³ Nikhef National Institute for Subatomic Physics and VU University Amsterdam, Amsterdam, The Netherlands
³⁴ Faculty of Physics and Applied Computer Science, AGH-University of Science and Technology, Kraków, Poland
³⁵ Henryk Niewodniczanski Institute of Nuclear Physics Polish Academy of Sciences, Kraków, Poland
³⁶ National Center for Nuclear Research (NCBJ), Warsaw, Poland
³⁷ Horia Hulubei National Institute of Physics and Nuclear Engineering, Bucharest-Magurele, Romania
³⁸ Petersburg Nuclear Physics Institute NRC Kurchatov Institute (PNPI NRC KI), Gatchina, Russia
³⁹ Institute for Nuclear Research of the Russian Academy of Sciences (INR RAS), Moscow, Russia
⁴⁰ Institute of Nuclear Physics, Moscow State University (SINP MSU), Moscow, Russia
⁴¹ Institute of Theoretical and Experimental Physics NRC Kurchatov Institute (ITEP NRC KI), Moscow, Russia
⁴² Yandex School of Data Analysis, Moscow, Russia
⁴³ Budker Institute of Nuclear Physics (SB RAS), Novosibirsk, Russia
⁴⁴ Institute for High Energy Physics NRC Kurchatov Institute (IHEP NRC KI), Protvino, Russia
⁴⁵ ICCUB, Universitat de Barcelona, Barcelona, Spain
⁴⁶ Instituto Galego de Física de Altas Enerxías (IGFAE), Universidade de Santiago de Compostela, Santiago de Compostela, Spain
⁴⁷ Instituto de Fisica Corpuscular, Centro Mixto Universidad de Valencia-CSIC, Valencia, Spain
⁴⁸ European Organization for Nuclear Research (CERN), Geneva, Switzerland
⁴⁹ Institute of Physics, Ecole Polytechnique Fédérale de Lausanne (EPFL), Lausanne, Switzerland
⁵⁰ Physik-Institut, Universität Zürich, Zurich, Switzerland
⁵¹ NSC Kharkiv Institute of Physics and Technology (NSC KIPT), Kharkiv, Ukraine
⁵² Institute for Nuclear Research of the National Academy of Sciences (KINR), Kyiv, Ukraine
⁵³ University of Birmingham, Birmingham, UK
⁵⁴ H.H. Wills Physics Laboratory, University of Bristol, Bristol, UK
⁵⁵ Cavendish Laboratory, University of Cambridge, Cambridge, UK
⁵⁶ Department of Physics, University of Warwick, Coventry, UK
⁵⁷ STFC Rutherford Appleton Laboratory, Didcot, UK
⁵⁸ School of Physics and Astronomy, University of Edinburgh, Edinburgh, UK
⁵⁹ School of Physics and Astronomy, University of Glasgow, Glasgow, UK
⁶⁰ Oliver Lodge Laboratory, University of Liverpool, Liverpool, UK
⁶¹ Imperial College London, London, UK
⁶² Department of Physics and Astronomy, University of Manchester, Manchester, UK
⁶³ Department of Physics, University of Oxford, Oxford, UK
⁶⁴ Massachusetts Institute of Technology, Cambridge, MA, USA
⁶⁵ University of Cincinnati, Cincinnati, OH, USA
⁶⁶ University of Maryland, College Park, MD, USA
⁶⁷ Los Alamos National Laboratory (LANL), Los Alamos, USA
⁶⁸ Syracuse University, Syracuse, NY, USA
⁶⁹ School of Physics and Astronomy, Monash University, Melbourne, Australia, *associated to*⁵⁶
⁷⁰ Pontifícia Universidade Católica do Rio de Janeiro (PUC-Rio), Rio de Janeiro, Brazil, *associated to*²
⁷¹ Physics and Micro Electronic College, Hunan University, Changsha, China, *associated to*⁷
⁷² Guangdong Provincial Key Laboratory of Nuclear Science, Guangdong-Hong Kong Joint Laboratory of Quantum Matter, Institute of Quantum Matter, South China Normal University, Guangzhou, China, *associated to*³
⁷³ School of Physics and Technology, Wuhan University, Wuhan, China, *associated to*³
⁷⁴ Departamento de Fisica , Universidad Nacional de Colombia, Bogotá, Colombia, *associated to*¹³
⁷⁵ Universität Bonn-Helmholtz-Institut für Strahlen und Kernphysik, Bonn, Germany, *associated to*¹⁷
⁷⁶ Institut für Physik, Universität Rostock, Rostock, Germany, *associated to*¹⁷
⁷⁷ Eotvos Lorand University, Budapest, Hungary, *associated to*⁴⁸

- ⁷⁸ INFN Sezione di Perugia, Perugia, Italy, *associated to*²¹
⁷⁹ Van Swinderen Institute, University of Groningen, Groningen, The Netherlands, *associated to*³²
⁸⁰ Universiteit Maastricht, Maastricht, The Netherlands, *associated to*³²
⁸¹ National Research Centre Kurchatov Institute, Moscow, Russia, *associated to*⁴¹
⁸² National Research University Higher School of Economics, Moscow, Russia, *associated to*⁴²
⁸³ National University of Science and Technology “MISIS”, Moscow, Russia, *associated to*⁴¹
⁸⁴ National Research Tomsk Polytechnic University, Tomsk, Russia, *associated to*⁴¹
⁸⁵ DS4DS, La Salle, Universitat Ramon Llull, Barcelona, Spain, *associated to*⁴⁵
⁸⁶ Department of Physics and Astronomy, Uppsala University, Uppsala, Sweden, *associated to*⁵⁹
⁸⁷ University of Michigan, Ann Arbor, USA, *associated to*⁶⁸

^a Universidade Federal do Triângulo Mineiro (UFTM), Uberaba, MG, Brazil

^b Hangzhou Institute for Advanced Study, UCAS, Hangzhou, China

^c Università di Bari, Bari, Italy

^d Università di Bologna, Bologna, Italy

^e Università di Cagliari, Cagliari, Italy

^f Università di Ferrara, Ferrara, Italy

^g Università di Firenze, Florence, Italy

^h Università di Genova, Genoa, Italy

ⁱ Università degli Studi di Milano, Milan, Italy

^j Università di Milano Bicocca, Milan, Italy

^k Università di Modena e Reggio Emilia, Modena, Italy

^l Università di Padova, Padua, Italy

^m Scuola Normale Superiore, Pisa, Italy

ⁿ Università di Pisa, Pisa, Italy

^o Università della Basilicata, Potenza, Italy

^p Università di Roma Tor Vergata, Rome, Italy

^q Università di Siena, Siena, Italy

^r Università di Urbino, Urbino, Italy

^s MSU-Iligan Institute of Technology (MSU-IIT), Iligan, Philippines

^t Faculty of Computer Science, Electronics and Telecommunications, AGH-University of Science and Technology, Kraków, Poland

^u P.N. Lebedev Physical Institute, Russian Academy of Science (LPI RAS), Moscow, Russia

^v Novosibirsk State University, Novosibirsk, Russia

^w Hanoi University of Science, Hanoi, Vietnam